ERROR PROPAGATION ANALYSIS IN THE PROCESSING OF SAR IMAGES FOR SUBSIDENCE MEASUREMENTS

THESIS ADVISORS:
Prof. J. Jordi Mallorqui, Universidad Politecnica de Catalunya
Prof. Giampiero Naletto, Università degli Studi di Padova

AUTHOR: Paolo Testolina

A.A. 2017-2018

UNIVERSITÀ DEGLI STUDI DI PADOVA

DEPARTMENT OF INFORMATION ENGINEERING

UNIVERSITAT POLITECNICA DE CATALUNYA

DEPARTMENT OF SIGNAL THEORY AND COMMUNICATIONS

ERROR PROPAGATION ANALYSIS IN THE PROCESSING OF SAR IMAGES FOR SUBSIDENCE MEASUREMENTS

THESIS ADVISORS:

Prof. J. Jordi Mallorqui, Universidad Politecnica de Catalunya

Prof. Giampiero Naletto, Università degli Studi di Padova

AUTHOR: *Paolo Testolina*

Padova, 1 October, 2018

Index

List of Figures

List of Tables

Abstract

Every measurement of the physical world is affected by uncertainty, no matter how precise the available instruments are. In other words, a measure completely free of errors is not possible. Being able to quantify this uncertainty, or, equivalently, the distribution of the errors is of the most fundamental importance, as it determines the validity of any experiment or procedure.

The Coherent Pixel Technique (CPT) is a technique developed by the Remote Sensing Laboratory (RSLab) of Universidad Politécnica de Catalunya (UPC) for the interferometric processing of satellite data. The objectives of CPT are the generation of altimetry and land displacement velocity maps, starting from the Synthetic Aperture Radar (SAR) acquisitions. The phase of these complex images already contains topographic information on the illuminated area. From it, the Persistent Scatter Interferometry (PSI) methodology allows the creation of deformation velocity maps over the interest area.

This work studies in depth part of the CPT technique, in the context of terrain deformation analysis. In particular, it is necessary for the final user to have a measure of the uncertainty on the results. This work addresses the problem for the specific case of the CPT, providing maps of the uncertainty that help to determine the reliability of each pixel.

Chapter 1

Introduction

Remote Sensing (RS) is a wide field of engineering that conjugates signal processing, antenna theory and physics to get information on objects without the need for a physical contact. Remote sensing techniques have a broad spectrum of applications, ranging from medicine to geoscience. Focusing on the latter, the scope of this thesis is the interferometric processing of satellite images through which data on the terrain deformation and topography can be obtained.

Many European and international spaceborne missions have been active for several decades and the constellations of satellites that constantly monitor the Earth have been increasing in number. This gives access to governments and organizations to data on the salinity of the oceans, on the sole humidity, on land subsidence in high risk zones such as mines, fracking sites, areas hit by landslides and earthquakes and on the structural integrity of bridges and buildings in general.

In this section a brief and general introduction on basic RS concepts is given, followed by an overview of the structure of the thesis.

The RS techniques can be grouped in two main categories, according to their working principle:

- Passive RS: the sensor collects information on the target environment passively, i.e., without radiating any wave. This method allows to investigate the radiometric characteristics of the objects, leading for instance to humidity and sole composition analysis or to ocean salinity measurements;

- Active RS: the sensor emits electromagnetic waves in the direction of the target in order to retrieve information by analysing the reflected wave. Topographic mapping and ground deformation monitoring are two of the main applications. For these applications, Radio Detection and Ranging (Radar) systems occupy a special place among the active sensors.

As this work deals with topographic measurements, only radars will be considered.

The main parameters that are used in topographic studies are

- for static scenarios, terrain elevation. The altimetry maps are called Digital Elevation Models (DEM) and can be obtained exploiting the phase difference in the backscattered signals through a technique called interferometry, that will be briefly analyzed in the following chapter;

- for dynamic scenarios, subsidence or uplifting velocity. Among the different available techniques, the focus will be on the Persistent Scatterer Interferometry (PSI), also known as Differential SAR Interferometry (DInSAR), that allows velocity measurements by comparing two interferometric images.

All PSI processing chains allow also the retrieval of a third parameter, the DEM error, that quantifies the error on the elevation model.

As in any parameter estimation, the results of this algorithm - the ground velocity and the DEM error - present a level of uncertainty, usually mathematically characterized through the standard deviation. The main objective of this work is to quantify the uncertainty or error on the velocity and DEM error. On one hand, this allows the final user to obtain a measure of reliability on the results provided by CPT, identifying the candidate pixels to be discarded. On the other hand, the analysis of the distribution of the standard deviation in relation to the topography of the processed pixels brings some insights of what are the most important parameters to take into account when using the PSI algorithms.

The structure of the thesis can be divided in two main parts: the first 4 chapters explain the underlying principles of interferometry and PSI as well as the functioning of the CPT algorithm. The last two chapters present the analysis of the error propagation through the algorithm, introducing first the general theory of uncertainty propagation, followed by its application to the specific algorithm and concluding with the testing on a simulated and on a realistic scenario. The chosen area for the experimental evaluation is the city of Venice, that presents some interesting topographic characteristics.
More specifically,

- Chapter 2 starts by introducing the Synthetic Aperture Radar (SAR) technique, a fundamental concept that makes the acquisition of images through small antennas, and therefore through spaceborne radars, feasible. Without giving all the details, the interferometry and PSI techniques are then presented.

- In Chapter 3 the analysis of the interferometric phase is carried out. As it will become clear throughout the following chapters, the phase is the most important parameter in the interferometric processing as all the information that need to be estimated can be recovered from it.

- Chapter 4 gives an outline of the CPT algorithm, fundamental for the understanding of the procedures and obtained results.

- Chapter 5 introduces the theoretical framework for the propagation of the error through the operations that are performed on the data in the CPT processing chain. The derived mathematical tools are then applied specifically to the various steps of the algorithm, obtaining for each the output covariance matrix from the input one. A first validation of the theoretical results is performed on a simulated scenario.

- Finally, in Chapter 6 the software developed in the previous pages is tested on a real environment, the city of Venice, that suffers of a slow subsidence and presents a particular and interesting topology.

Chapter 2

Synthetic Aperture Radars and Interferometry bases

This chapter outlines the motivation behind and the general principles of the Synthetic Aperture Radars. The geometry of the considered scenario and the general methodology that allows the retrieval of useful information from the SAR raw data are presented.

After a brief list of the different acquisition modes, the distortions due to the geometric characteristics of the environment are briefly presented. Finally, the basic ideas behind standard and differential interferometric processing are presented.

2.1 System description

As the name "RAdio Detection And Ranging" suggests, radars work as range measuring devices. Although it may appear like a trivial task, from distance measurements several information can be obtained after the proper processing, as it will become clear along the development of this thesis.

As already mentioned, active remote sensing acquires data by emitting an electromagnetic pulse and analyzing thereafter the backscattered response of the targets. Consider a sensor mounted on an aircraft or on a satellite. The direction along which the sensor moves is called azimuth and the one orthogonal to it range. In particular, it is possible to distinguish between slant and ground range, the former being the direction travelled by the radiated pulse and the latter its projection on the ground plane. Figure 2.1 clarifies the geometry of the system.

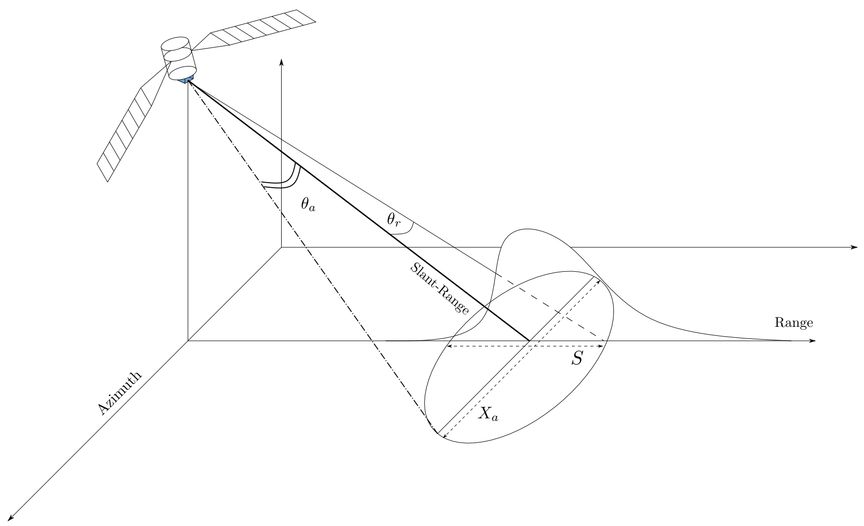

Figure 2.1: SAR acquisition geometry.

This kind of Radar sensors is called Side Looking Real Aperture Radar (SLAR). Starting with a brief analysis of the SLAR functioning principles, it is possible to build the theoretical foundations of the more advanced SAR technique and the motivations behind it.

The area illuminated by the radiated wave is called *footprint* of the antenna. The subsequent footprints trace the *swath*, i.e., the area acquired by the antenna as it moves. The dimensions of its axes, namely S in range and X_a in azimuth, depend on the radiation pattern of the antenna. Observing the geometry of the system as depicted in figure 2.1, goniometric considerations lead to

$$\begin{cases} S \approx \frac{h\theta_r}{\cos^2(\theta)} \\ X_a \approx \frac{h\theta_a}{\cos(\theta)} \end{cases} \tag{2.1}$$

being h the height of the satellite, θ_r and θ_a the antenna beamwidth in the range and azimuth direction respectively and θ the off-nadir or look angle.

Considering two targets separated by a distance Δr in the range direction as in figure 2.2, the waves they reflect, called echoes, are separated in time by

$$\Delta t = 2\frac{\Delta p}{c} = 2\frac{\Delta r \sin(\theta)}{c} \tag{2.2}$$

being Δp the difference of the paths length.

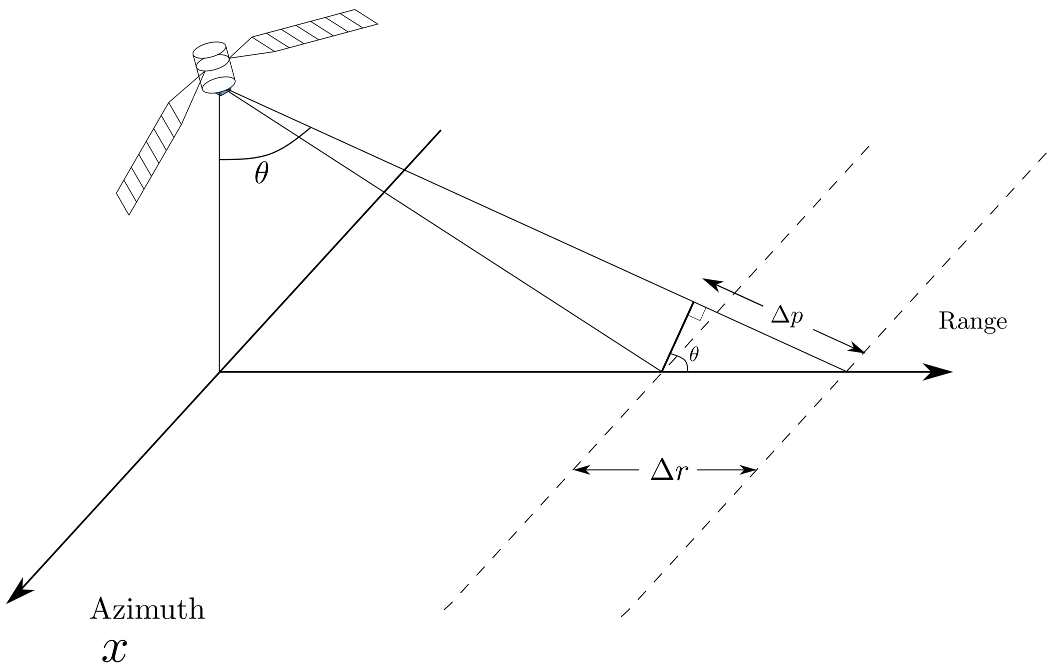

Figure 2.2: Range resolution geometry.

Using pulses of duration T, the maximum resolution Δr_{min} in the range direction corresponds to the minimum time separation between the echoes of the two objects before overlapping and is

$$T = 2\frac{\Delta r_{min} \sin(\theta)}{c} \implies \Delta r_{min} = \frac{T}{2\sin(\theta)}c \tag{2.3}$$

Using the pulse bandwidth B as reference, $T \approx 1/B$ leads to reasonable resolutions, in the order of meters.

The azimuth resolution depends on the footprint dimension along the azimuth direction. For an antenna of length L transmitting pulses at frequency $f = \frac{c}{\lambda}$

$$X_a \approx \frac{h\lambda}{L}\cos\theta \tag{2.4}$$

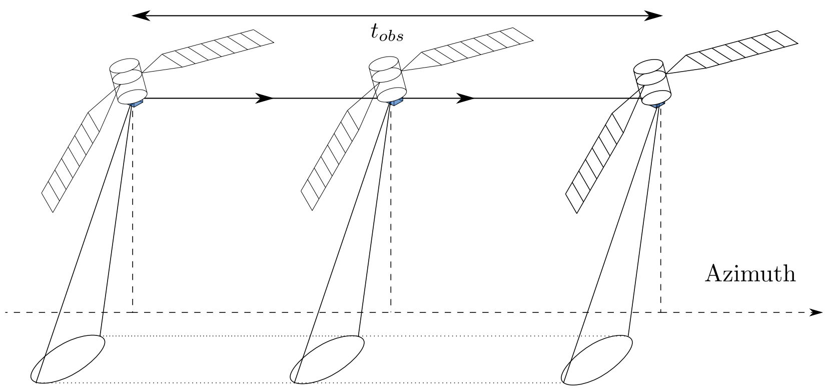

Figure 2.3: Sensor pass-by.

Considering typical incidence angles ($20° - 50°$) and L-band frequencies, a good azimuth resolution, comparable to the range one, can be obtained with an antenna of dimension L in the order of kilometers. It is then clear that Real Aperture Radars are not a feasible option for spaceborne systems.

The idea behind the Synthetic Aperture Radar is to be able to synthetize the large aperture required for a good azimuth resolution using antennas of standard dimensions. Two approaches are possible: one, using an array of antennas (spatial multiplexing), and the other using a moving antenna (temporal multiplexing). Either way, the data received at each sensor need to be processed to coherently combine the single aquisitions and obtain a final high resolution image. In the second case, that is the one of interest for this study and in general for spaceborne settings, the combining techniques are called focusing algorithms as they deal with placing the targets in the correct locations in the image plane. Note that coherent combination requires, by definition, the radar echoes to be correlated, that is the case if they are the result of the interaction with the same scatterers or set of scatterers from similar observation conditions. Moreover, the radars employed in interferometric applications need to be coherent, i.e., they should provide an extremely precised control on the phase of the emitted pulses. In the large majority of the cases, the signals are required to have the exact same phase information when they are transmitted in the target direction.

Clearly, several acquisition techniques are possible according to the steering of the antenna during the pass over the target area, and the combining methods differ accordingly. In the next section a brief overview of the acquisition modes is given while one on the combining algorithms are beyond the scope of this thesis.

Referring to figure 2.3, the synthetized length of the antenna is $L' = v \cdot t_{acq}$, where v is the velocity of the platform and t_{acq} is the time during which the target is

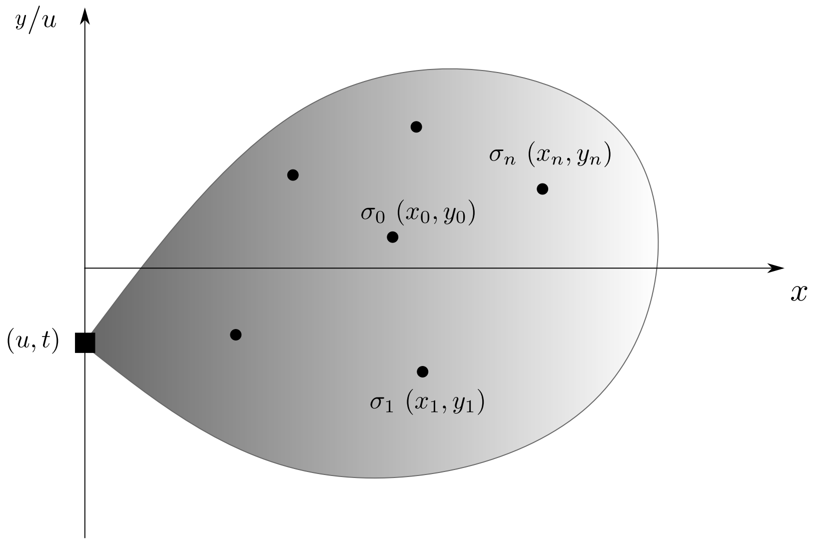

Figure 2.4: Target plane and acquisition scenario.

illuminated. The synthetic length can be stretched to obtain higher resolutions in the azimuth direction at the cost of a higher combination complexity: the upper limit to the azimuth resolution or, equivalently, to the synthetic length, is set by the focusing algorithms and by the related errors.
Aside from the focusing, several other procedures are necessary to estimate precisely the position of the satellite and its trajectory as well as to compensate the effects related to the radiation pattern of the antenna. The following section offers a brief explanation of the main ideas that are behind the extraction of useful information from the data received at the antenna, referred to as raw data.

2.2 Raw data processing

Differently from optical sensors, the raw data acquired by SAR systems doesn't offer any useful visualization. In this section a brief mathematical analysis describes the structure of the signals involved in the SAR imaging systems and the problems related to the focusing algorithms.

Consider a general scenario as the one depicted in fig. 2.4, where the sensor moves along the u axis and n targets are distributed in the (x, y) plane. Note that the u and y axes coincide, but two symbols are used to take into account their different meanings. For simplicity, the targets are represented by point reflectors of reflectivity σ_i. Suppose that the radar illuminates an area with a large bandwidth signal $p(t)$. As the radar moves, it keeps radiating pulses in the direction of the target with a given Pulse Repetition Frequency (PRF). For simplicity, the antenna is assumed to be ominidirectional so the target is always illuminated.

The SAR sensors usually work with chirp signals, a cathegory of signals that are characterized by a time-dependent instantaneous frequency $f = \alpha t$, where α is known as chirp rate. For a pulse of duration τ, the signal bandwith is $B = \tau\alpha$, allowing the chirp signals to have an extremely large bandwidth without the strict constraints on the time duration that other kinds of signals would impose.
The backscattered signal received by the sensor at time t and azimuth position u is

$$s(t,u) = \sum_{i=1}^{n} \sigma_i p\left[t - \tau_i^{del}(u)\right] \tag{2.5}$$

where $\tau_i^{del}(u)$ is the (2-way) round trip delay of the signal reflected by the i-th target, that varies with the position of the sensor according to

$$\tau_i^{del}(u) = 2\frac{\sqrt{x_i^2 + (y_i - u)^2}}{c} \tag{2.6}$$

Clearly, the same dependance on the relative position between the sensor and the target can be found also in the range slant-range coordinate of the target, that changes as the platform moves:

$$R_i(u) = \sqrt{x_i^2 + (y_i - u)^2} = c\frac{\tau_i^{del}(u)}{2} \tag{2.7}$$

$R_i(u)$ is minimum when $u = y_i$, that is, when the azimuth position of the sensor coincides with the y coordinate of the target. This point is called Closest Point of Approach (CPA). As shown in fig. 2.5 the (u,t) plane, the slant-range distance $R_i(u)$, or, equivalently, the time delay $\tau_i^{del}(u)$, for the i-th target describes a half-hyperbola that causes the Range Cell Migration (RCM), i.e., the response of a target appears in different resolution cells. This complicates the processing, as the signals received from different targets overlap. This is the main factor that makes the raw data image unreadable by its own.

Several techniques exist that can separate and remap the target responses to the proper resolution cells. One of the most basic is the two dimensional filtering: first, a filter is applied in the range direction, performing the so called "range compression". A second filter is then applied in the azimuth domain, taking into account the already mentioned RCM that complicates the processing. Usually, filtering is performed in the frequency domain to minimize the computational load.

The final product of the overall processing is a complex-valued image called Single Look Complex (SLC). For a single target, defining $A \in \mathbb{R}$ as the amplitude and Φ as the phase, the mathematical expression of the backscattered signal after the focusing is

$$V = Ae^{j\Phi} \tag{2.8}$$

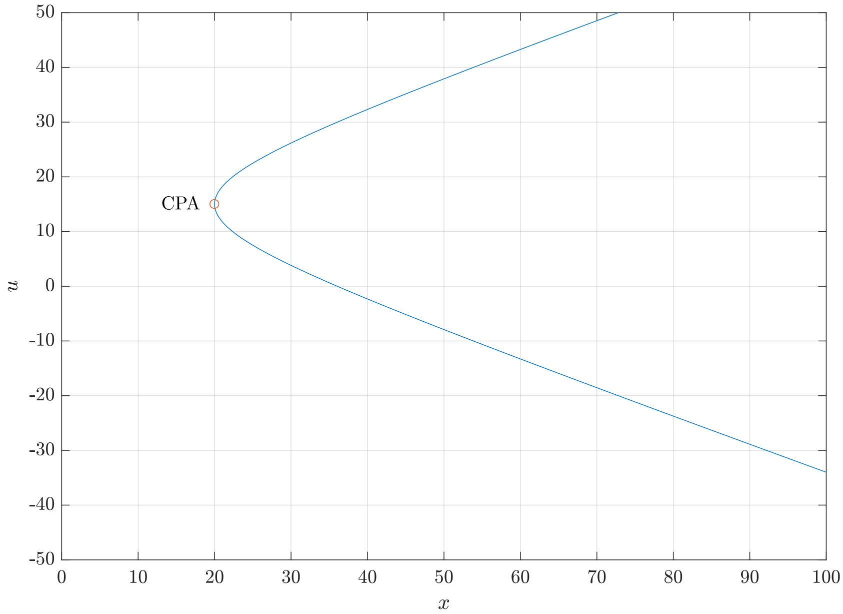

Figure 2.5: The slant-range distance plotted on the (x, u) plane. The axes are expressed in normalized distance units. The considered target is in position $(10, 15)$ in the (x, y) plane.

For a platform transmitting a pulse at frequency $f = c/\lambda$ at distance R from the target the phase can be expressed:

$$\Phi = -\frac{4\pi}{\lambda}R + \psi_{scatterer} \tag{2.9}$$

where $\psi_{scatterer}$ is a phase term related to the physical property of the reflecting object. It can be already observed how the phase term contains useful information.

2.3 Overview on the different acquisition modes

As already mentioned, several configurations are available for the acquisition of data on the target area. In this section, some of the most common acquisition modes are briefly presented.

- Stripmap: in this mode the azimuth angle is kept constant as the satellite moves along its track. The ground swath is illuminated by a continuous sequence of pulses, resulting in a continous along track image quality (fig. 2.6).

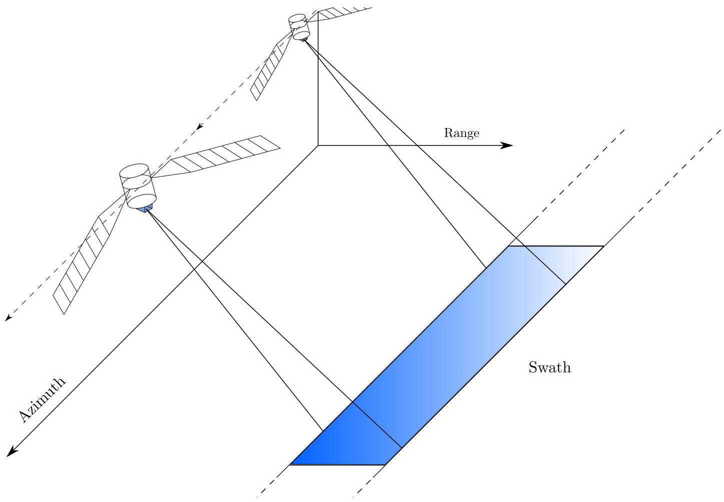

Figure 2.6: Stripmap acquisition.

- Spotlight (SPOT): the azimuth resolution is improved by steering the angle in order to keep illuminating the target while the satellite moves, obtaining a larger angular extent of the illumination, or, equivalently, synthetizing a larger aperture. Note that the steering is done in the direction opposite to the platform movement (fig. 2.7).

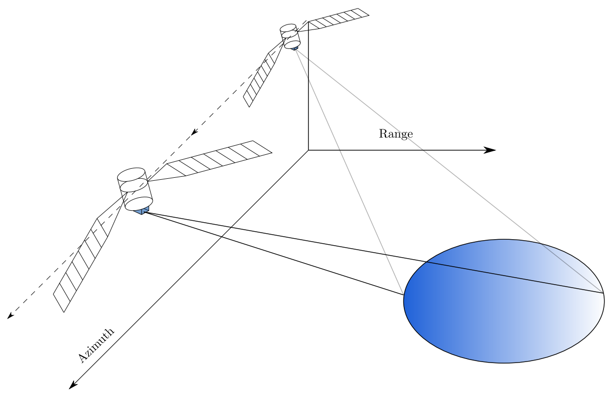

Figure 2.7: Spotlight acquisition.

- Scanning SAR (ScanSAR): the antenna acquires several adjacent images, called bursts, in the range direction during the pass, obtaining a larger swath with degraded azimuth resolution. The bursts that have the same incident angle form a subswath, and the parallel subswaths form the extended swath.

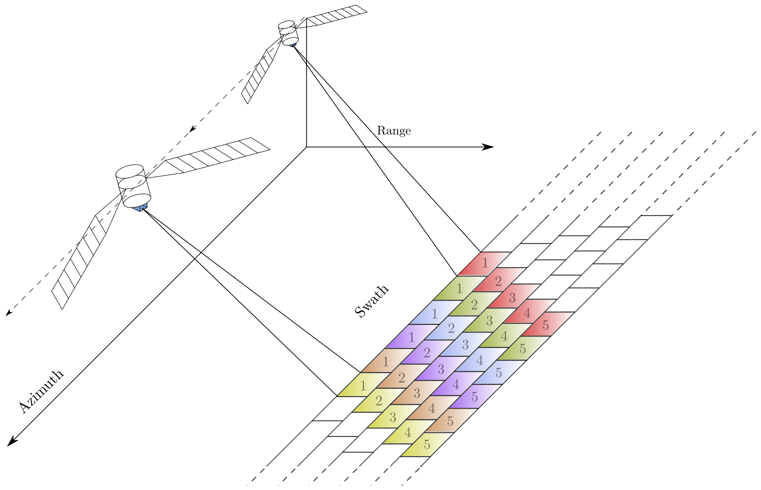

Figure 2.8: Scansar acquisition with five subswaths. The numbers indicate the order of the bursts.

- Terrain Observation by Progressive Scans (TOPS) is a type of acquisition mode derived from ScanSAR. Similarly to the ScanSAR, the data is acquired in parallel subswaths. The main difference is that during the acquisition the antenna is electronically steered not only in the range direction but also in the along track direction, in the opposite direction with respect to the SPOT mode (hence the name TOPS). This worsens the azimuth resolution but almost completely solves the problems of the ScanSAR mode, like the scalloping and the non constant azimuth resolution.

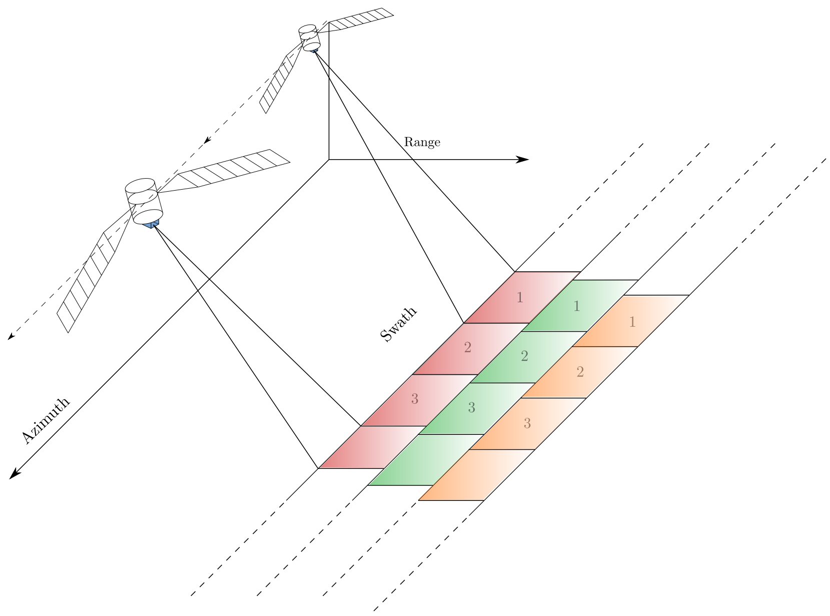

Figure 2.9: TOPS acquisition with 3 subswaths. The numbers indicate the order of the bursts. Firstly, the antenna is electronically rotated in the direction in which the platform moves, scanning part of a subswath with consecutive burst, in this case three. Secondly, the angle of incidence is changed to the following subswath, in the figure indicated by a different color. After having completed the acquisition for all the subswaths, the process starts from the beginning.

2.4 Geometric distortions

SAR techniques suffer of some distortions related to the geometry intrinsic in the acquisition setup. Although they are not part of the error analysis of this work, it is worth to briefly mention them as possible causes of problems.

As discussed at the beginning of the first section of this chapter, the main information retrieved by the satellite sensor is the distance of the targets. For this reason in all acquired images the target's image position is shifted due to its elevation. The target scene is projected to the so-called slant-range geometry. According to its name, the radar measures distances; the elements of the scene are then ordered as "seen" by the sensor, in increasing distances. A SAR image, after the proper processing, may look similar to an optical one, with some important differences. The main geometric distortions typical of a SAR image are now briefly presented and the corresponding images try to clarify the concepts according to this reasoning.
The main geometric distortions are

- **foreshortening**: it occurs when the radar signal reaches an object that has a slope facing toward the radar as in Fig. 2.10. In this case, the length of the slope would appear compressed and the target bright due to the strong reflection.

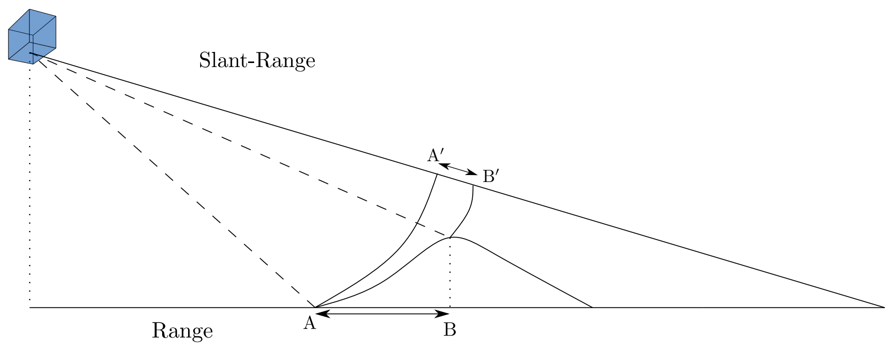

Figure 2.10: Foreshortening geometry.

- **layover**: in the presence of very steep terrain, with slope larger than the angle of incidence as in Fig. 2.11, the backscattered radiation from the top reaches the radar before the one from the bottom, resulting in an inversion of the two points.

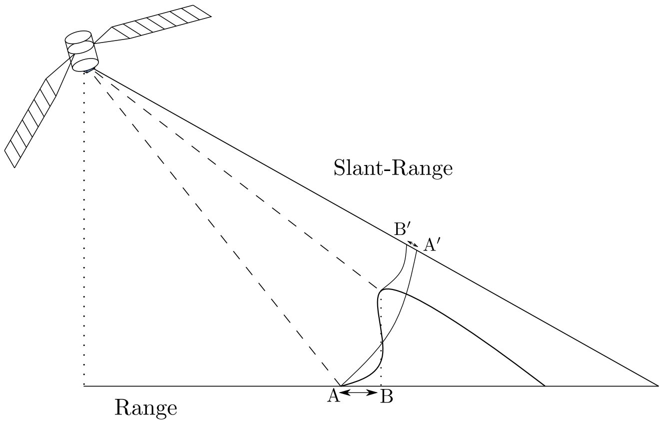

Figure 2.11: Layover geometry.

- **shadowing**: in opposition to the foreshortening, the slope is not illuminate by the radar, as depicted in Fig. 2.12. This results in dark or void areas in the images.

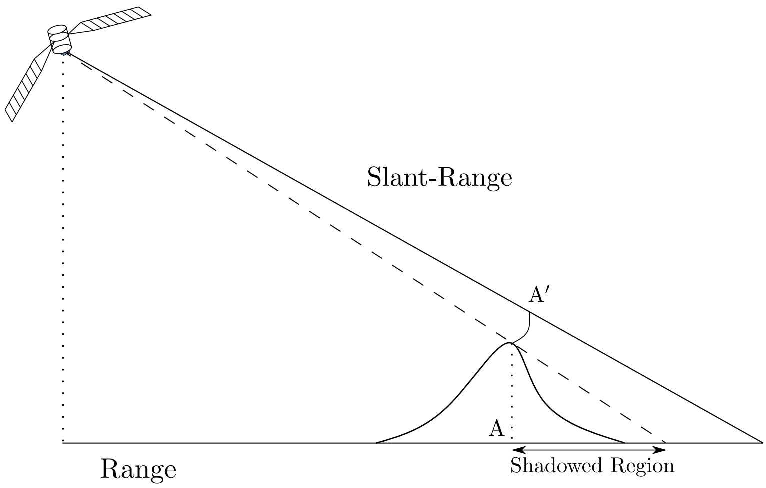

Figure 2.12: Shadowing geometry.

As already said, these distortions are deterministic and have been extensively studied. The focus of the thesis is rather on the stochastic errors that affect any kind of measurements and their propagation in the processing described in the following.

2.5 SAR Interferometry

Interferometry is a general concept that can be found in different fields, ranging from astronomy to biology. The basic idea is to superimposed coherent signals in order to obtain information on them exploiting their phase difference. In the specific case of SAR, this is applied to the SLC images obtained from the already mentioned processing.

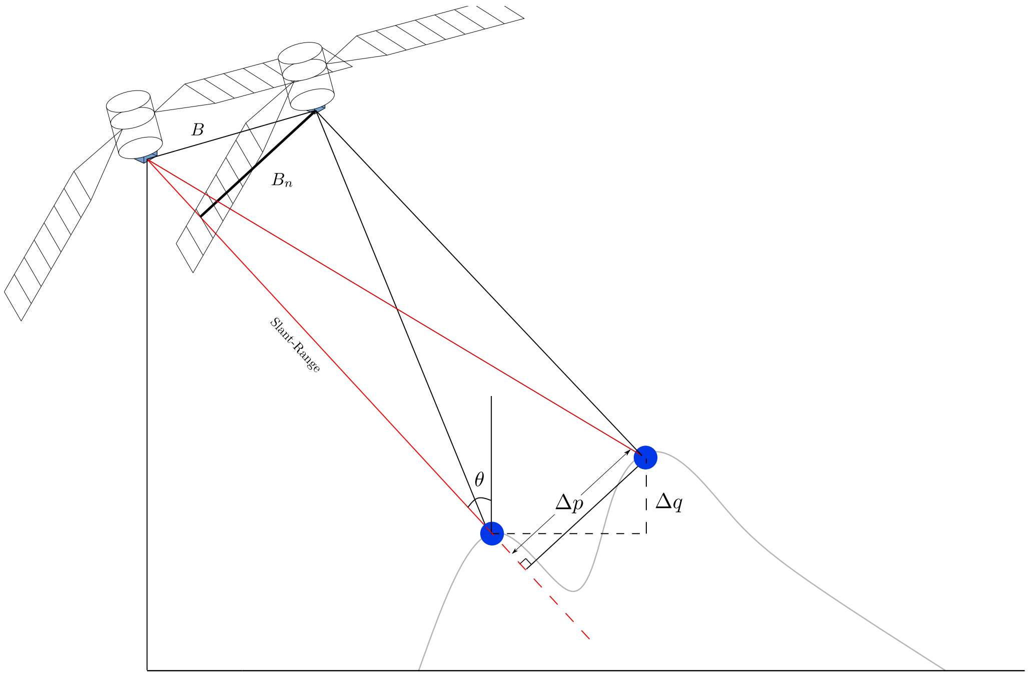

Figure 2.13: Geometry of the considered scenario.

Let S_i, S_j be two SLC images acquired by the platform from two slightly different positions, separated by a distance called interferometric baseline and at two different times T_i, T_j. The considered geometry is pictured in Fig. 2.13. For simplicity, assume that in each resolution cell only a point scatterer is present, that is, only a target with high omnidirectional and uniform reflectivity that is stable in time. The useful parameters for the interferometric processing are the spatial or perpendicular baseline B_n, i.e. the normal distance between the platform positions, the radar-to-target distance R_0, the distance between targets along the perpendicular to the slant-range direction Δp and their altitude difference Δq.

In this scenario, the corresponding interferogram is obtained as

$$I_{i,j} = S_i S_j^* \tag{2.10}$$

where the Hermitian product is performed pixelwise. From eq. (2.8), the interferometric complex signal is

$$V_{i,j} = A_i A_j e^{\Phi_i - \Phi_j} = A_{i,j} e^{\phi_{i,j}} \tag{2.11}$$

where the phase variation from one resolution cell to the adjacent one is expressed using eq. (2.9) as

$$\phi_{i,j} = -\frac{4\pi}{\lambda}(R_i - R_j) + \psi_{scatterer,i} - \psi_{scatterer,j} \tag{2.12}$$

Supposing that the two targets in the two resolution cells share the same backscattering properties, that is a well verified hypothesis in presence of point scatterers, the two phase contributions $\psi_{scatterer,i}$, $\psi_{scatterer,j}$ cancel out. Therefore the interferometric phase can be written, using the previously defined parameters, as

$$\phi_{i,j} = \Delta\Phi = -\frac{4\pi}{\lambda}(R_i - R_j) \approx -\frac{4\pi}{\lambda}\frac{B_n \Delta p}{R_0} \tag{2.13}$$

Decomposing the targets height difference Δp in the slant-range and in the vertical direction

$$\Delta p = \frac{\Delta p}{\sin\theta} + \frac{\Delta p}{\tan\theta} \tag{2.14}$$

the phase expression becomes:

$$\phi_{i,j} = -\frac{4\pi}{\lambda}\frac{B_n \Delta q}{R_0 \sin\theta} - \frac{4\pi}{\lambda}\frac{B_n \Delta p}{R_0 \tan\theta} = \phi_{flat} + \phi_{alt} \tag{2.15}$$

where ϕ_{flat} is the so called "flat-Earth term", that can be cancelled thanks to precise orbital localization and baseline estimation (interferogram flattening), whereas ϕ_{alt} contains the information about the altitude variation between the two targets and can be used to generate *Digital Elevation Model*s (DEM). Due to the cyclic nature of the phase, altitude ambiguities arise: consider a height difference Δh between two targets in adjacent resolution cells. For $\Delta h > \frac{\lambda R \sin\theta}{2B_n}$ a variation of $2k\pi$ is registered, with $k \in \mathbb{Z}$ being the number of complete 2π cycles. Therefore, an unwrapping procedure, i.e. the addition of the right number k of 2π cycles, is needed to remove the ambiguities of the ϕ_{alt} term and obtain the DEM.
Notice that up to this point no atmospheric nor phase noise contribution have been taken into account.

From an electromagnetic point of view, a simple model for the atmosphere is an infinite number of infinitesimal or extremely small layers with different scattering properties, that vary slowy from one layer to the next. These properties change in both the temporal and spatial dimensions at a very wide range of possible rates. A precise deterministic approach is not practical, and in most cases the atmospheric effects are modelled as random processes. This stack of layers is traversed by the pulse emitted by the radar on the way to the target and on the way back. The main consequence is that the backscattered signal reaches the radar with a random delay offset, that is caused by the different speeds of propagation in each of the medium and is generally known as Atmospheric Phase Screen (APS). As radars estimate the distances based on the received pulse delay, this random term, that can change from one acquisition to the next, degrades the performance of the system and may be considered as "atmospheric noise".

The complete expression of $\phi_{i,j}$ is thus

$$\phi_{i,j} = \phi_{flat} + \phi_{alt} + \phi_{atm} + \phi_{noise} \tag{2.16}$$

While having different causes, the atmospheric and the phase noise are usually both considered as disturbances. An in-depth analysis of their stochastic characterization is carried out in chapter 3 and 5.

2.6 PSI processing

This work narrows its scope on the Differential Interferometry SAR (DInSAR) or Persistent Scatterer Interferometry (PSI) processing. Among the several applications deriving from the analysis and the processing of SLC images and interferometers, terrain motion monitoring can be performed through PSI techniques. Once again the key parameter is the interferometric phase, that in presence of land deformation, e.g. after a landslide, an Earthquake or a vulcanic eruption or in subsiding or uplifting areas, registers an additive term proportional to the height variation between the two SLC acquisitions:

$$\phi_{def} = \frac{4\pi}{\lambda} d \tag{2.17}$$

where d is the projection of the target displacement on the slant-range direction. The objective of DInSAR is to estimate the variation magnitude d.
Fig. 2.14 clarifies the considered geometry.

Therefore, the overall interferometric phase is

$$\phi_{i,j} = \phi_{flat} + \phi_{alt} + \phi_{atm} + \phi_{noise} + \phi_{def} \tag{2.18}$$

After the flattening, the terrain motion term needs to be extracted from the residual phase. The atmosphere contribution has to be estimated in order to discriminate the displacement term from the atmospheric one. In presence of abrupt motion, as in the case of landslides or violent earthquakes, the ϕ_{def} can cause unwanted phase cycles. This happens if

$$d > \frac{\lambda}{2} \tag{2.19}$$

and a second unwrapping procedure is needed to determine the correct displacement in meters. Notice that the corresponding term does not depend on the spatial baseline between acquisitions, but by its very nature is strongly dependent on the temporal distance, called temporal baseline, between them. It is evident for instance that "fast" events can be detected with a short temporal baseline while

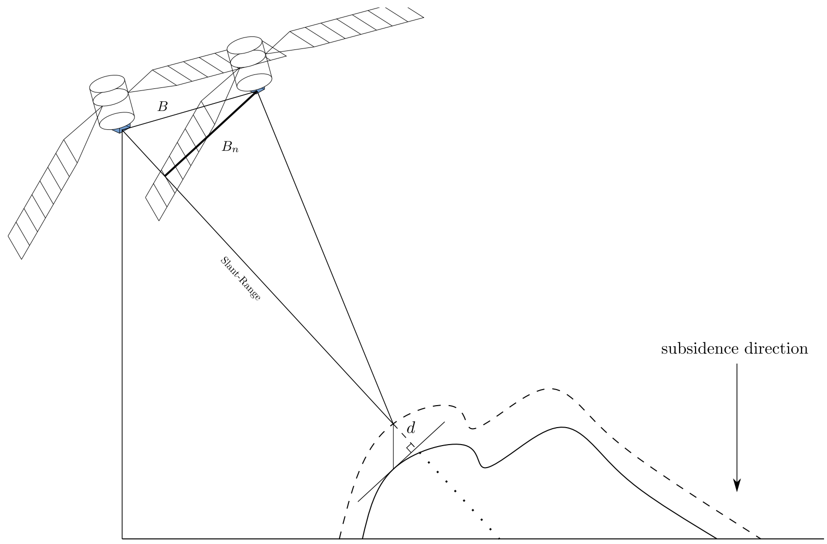

Figure 2.14: Acquisition geometry in presence of ground subsidence.

low velocity phenomena necessarily require a larger time span. This distinction is reflected in two different classes of DInSAR procedures, namely classic DInSAR and advanced DInSAR. The reason for this distinction resides in the fact that when using large temporal baselines new issues arise: for instance, the phase noise increases due to temporal decorrelation effects, as explained in the next chapter.

Chapter 4 gives a more technical and in-depth description of the PSI chain as implemented in the CPT software.

Chapter 3

Stochastic characterization of the interferometric phase noise

Given the considerations of the previous chapter, it is clear that the phase of the interferograms plays a fundamental role in the PSI processing. As explained, the useful interferometric phase can be written according to (2.18) as

$$\phi_{i,j} = \phi_{flat} + \phi_{alt} + \phi_{atm} + \phi_{noise} + \phi_{def} \rightarrow \phi_{i,j}^{PSI} = \phi_{noise} + \phi_{def} \qquad (3.1)$$

where the last expression is obtained through the already detailed procedures. Recalling that the PSI objective is to estimate the deformation, the residual phase can be interpreted using the classical signal plus addictive noise model, that is well known in the telecommunication and signal processing environments. In this chapter, the stochastic properties of the phase are analysed. This allows to introduce the main aleatory sources of errors, whose impact is propagated step by step through the CPT in chapter 5. Finally, a brief list of quality estimators is presented.

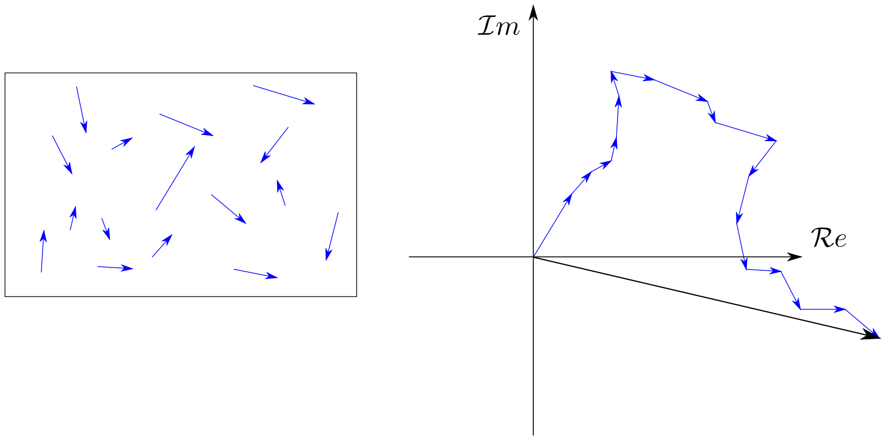

Figure 3.1: Phasors related to each scatterer in a resolution cell.

3.1 Statistics of a resolution cell

Starting from the very beginning of the processing, the complex probability density function (PDF) of a SAR resolution cell is derived. From it the PDF of an interferometric resolution cell is obtained and eventually the error distributions are analyzed.

3.1.1 Stochastic characterization

SAR resolution cell In SAR systems the size of a resolution cell is many orders of magnitude larger than the signal wavelength. This implies that a resolution cell may contain several targets with different backscattering properties, whose individual contribution cannot be identified. This is the case for the distributed scatterers, whose properties will be analysed in the following together with another kind of target, the point scatterer.

As each of the individual contributions is a complex value, a phasor visualization can help understanding the problem: as it can be observed in Fig. 3.1, the overall response is the result of the superposition of terms that, being highly unpredictable, can be considered fully random. This leads to the phenomenon known as *speckle*, i.e. the SAR images appearing "grainy". An example of speckle is reported in Fig. **??**, where the noise can be clearly observed. A common solution is to apply a multilook procedure, that sacrifices some resolution to cancel out the random contributions in order to obtain a cleaner image. Several multilook techniques exists, but in general they involve the inchoerent averaging of patches of resolution cells. In Fig. 3.2 the effect of the multilook is shown: on one hand the different resolution, and on the other, the great reduction of the speckle noise. More advanced techniques are available to decrease the noise the minimum resolution loss.
Mathematically, each small scatterer i accounts for a complex term in the reflected

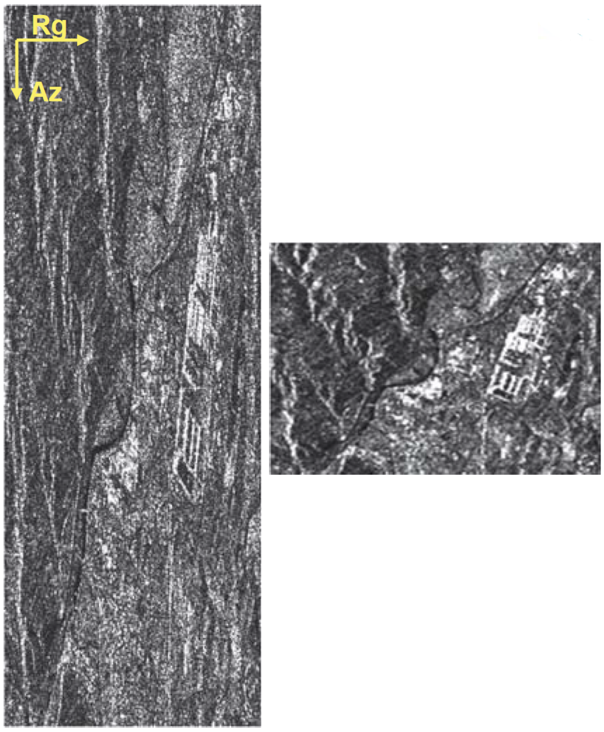

Figure 3.2: SLC phase before (left) and after (right) the application of multilook.

signal, this latter being the sum (superposition) of all of them:

$$\text{single scatterer: } A_i e^{j\psi_i} \implies \text{backscattered signal: } \sum_{i=0}^{N} A_i e^{j\psi_i} \tag{3.2}$$

Following this approach and considering each contribution in each SAR image as a random variable, it would be natural to derive the total response applying the central limit theorem. This can be done if the following assumptions hold [3]:

- No single dominant scatterer is present in a resolution cell. This is generally true for most of the natural scatterers;
- The phase of the scatterers are i.i.d. random variables uniformly distributed in $[-\pi;\pi]$;
- The phase and the amplitude of every scatterer are uncorrelated.

Under these conditions and considering the fact that the images are 2D complex random variables, the central limit theorem implies that the overall backscattered signal is distributed as a complex circular Gaussian variable, whose PDF is, being σ^2 the variance:

$$p(y) = \frac{1}{2\pi\sigma^2} e^{-\frac{(\Re(y))^2 + (\Im(y))^2}{2\sigma^2}} \tag{3.3}$$

that also implies that the real and imaginary part of y are uncorrelated. For $y = \Re(y) + \Im(y) = Ae^{j\psi}$ the PDFs for the amplitude and the phase can be derived finding first the joint distribution through the Jacobian

$$p(A,\psi) = \begin{cases} \frac{A}{2\pi\sigma^2} e^{-\frac{A^2}{2\sigma^2}} & \text{for } A \geq 0 \text{ and } -\pi \leq \psi < \pi \\ 0 & \text{otherwise} \end{cases} \tag{3.4}$$

and then, by marginalization, the amplitude PDF:

$$p(A) = \begin{cases} \frac{A}{\sigma^2} e^{-\frac{A^2}{2\sigma^2}} & \text{for } A \geq 0 \\ 0 & \text{otherwise} \end{cases} \tag{3.5}$$

and the phase PDF:

$$p(\psi) = \begin{cases} \frac{1}{2\pi} & \text{for } -\pi \leq \psi < \pi \\ 0 & \text{otherwise} \end{cases} \tag{3.6}$$

Note that the former is a Rayleigh distribution while the latter confirms the initial assumption of uniformity. Also, it appears clear from the expressions that the two random variables are uncorrelated.

Interferometric resolution cell As the interferograms are computed as in (2.10), their PDF is the distribution of the product of two circular Gaussian random variables S_i, S_j with zero mean and variance $\sigma_i = \sigma_j$. First, it is necessary to introduce the complex correlation coefficient (or complex coherence) γ between S_i and S_j, defined as

$$\gamma = \frac{E\left[S_i S_j^*\right]}{\sqrt{E\left[|S_i|^2\right] E\left[|S_j|^2\right]}} = |\gamma|\, e^{j\phi_0}. \tag{3.7}$$

Notice that the definition of coherence closely resembles the way to compute the interferograms: this implies that the phase ϕ_0 of the coherence represents the expected value of the interferometric phase. Therefore, it can be already observed how the coherence can be interpreted as a phase quality measure; in particular, as it will be clarified in the following chapters, the magnitude $|\gamma|$ is a measure of the phase noise.
Finally, note that the computation of the coherence involves expected values $E[\cdot]$, that in practice are rarely if not never available, as they require an infinite or large number of realizations with the exact same acquisition geometry. Several estimators exist for the coherence [5], [6], [7], under the assumptions that the images are stationary over time and ergodic over the same scenes.

In order to characterize the interferogram properties more precisely, the joint distribution of S_i and S_j is computed. It has been shown that, given a complex covariance matrix

$$C_y = E\left[\left[\begin{array}{cc} S_i^* & S_j^* \end{array}\right]\left[\begin{array}{c} S_i \\ S_j \end{array}\right]\right] = \left[\begin{array}{cc} \sigma_i^2 & \gamma\sqrt{E\left[|S_i|^2\right]E\left[|S_j|^2\right]} \\ \gamma^*\sqrt{E\left[|S_i|^2\right]E\left[|S_j|^2\right]} & \sigma_j \end{array}\right] \quad (3.8)$$

the joint distribution of S_i, S_j is

$$p\left(S_i, S_j\right) = \frac{1}{\pi^2\left|C_y\right|}e^{-\left[\begin{array}{cc} S_i^* & S_j^* \end{array}\right]C_y^{-1}\left[\begin{array}{c} S_i \\ S_j \end{array}\right]}. \quad (3.9)$$

Multilook procedures can be applied also at the interferogram level in order to reduce the interferometric phase noise. In this case, differently from the SLC multilook, the averaging is coherent. Several techniques are available. An example is reported in fig. 3.3 and fig. 3.4, where it is possible to observe the noisy interferometric phase and the subsequent reduction due to the multilook.

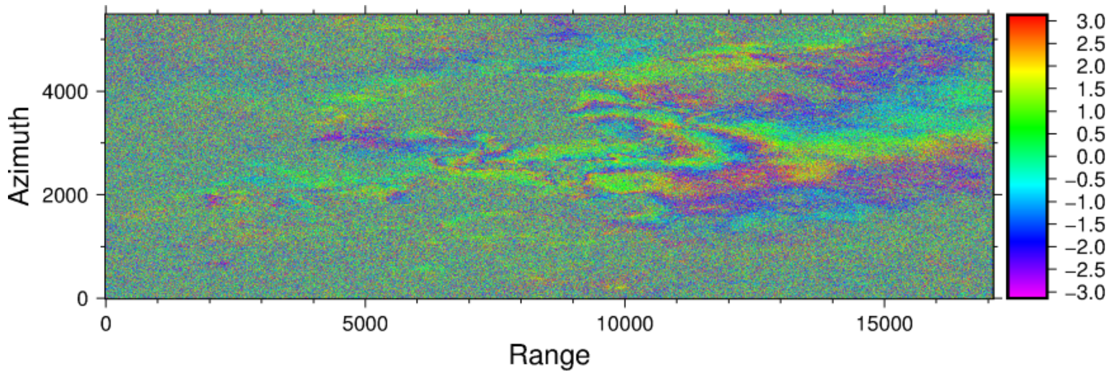

Figure 3.3: Interferometric phase over Mexico City. The image is obtained combining two SLCs (2017/06/07 and 2017/09/23) acquired by Sentinel 1. The resolution is 20 m/px in the azimuth and 5 m/px in the range direction.

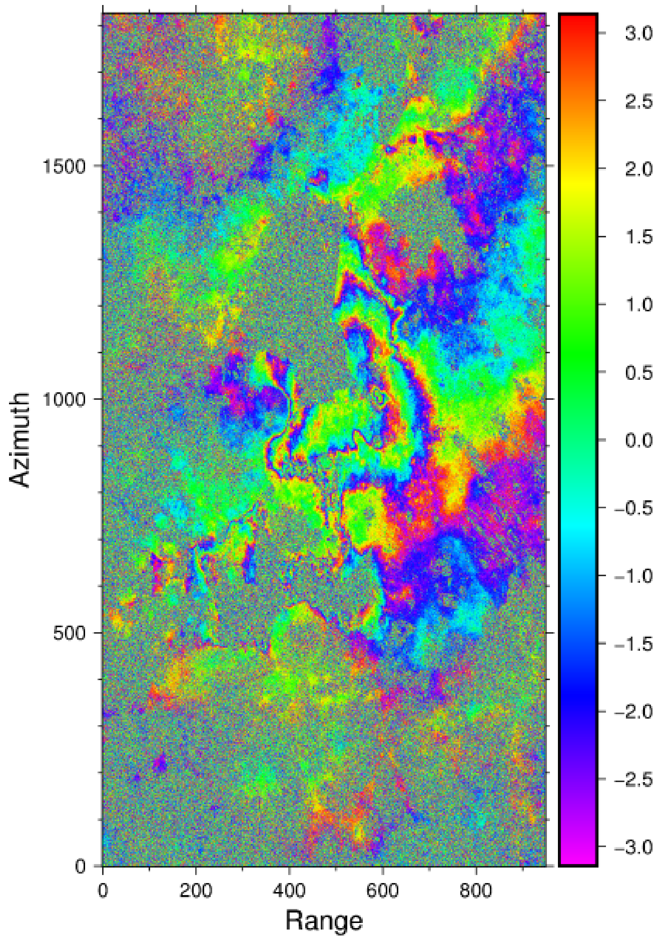

Figure 3.4: Interferometric phase after the application of a multilook factor of 3 in the azimuth and 5 in the range direction.

Considering also the effects on the PDF of a multilook factor L, as in the previous section the joint probability of the amplitude and phase of the interferometer can be found by using the Jacobian:

$$p\left(A_{i,j},\phi_{i,j}\right)= \\ =\frac{2L(LA_{i,j})^{L}}{\pi\zeta^{L+1}(1-|\gamma|^{2}\,\Gamma(L))}\exp\left(-\frac{2\,|\gamma|\,LA_{i,j}\cos\left(\phi_{i,j}-\phi_{0}\right)}{\zeta\left(1-|\gamma|^{2}\right)}\right)K_{L-1}\left(\frac{2LA_{i,j}}{\zeta\left(1-|\gamma|^{2}\right)}\right) \tag{3.10}$$

being the K_{L-1} the modified Bessel function of the third kind, Γ the Gamma function and $\zeta=\sqrt{E\left[|S_i|^2\right]E\left[|S_j|^2\right]}$. Finally, from (3.10) the phase distribution can be isolated by marginalization and its expression can be expressed more clearly using hypergeometric functions:

$$p(\phi_{i,j})= \\ =\frac{\Gamma(L+1/2)(1-\gamma^2)^L|\gamma|\cos(\phi-\phi_0)}{2\sqrt{\pi}\Gamma(L)(1-\gamma^2\cos^2(\phi-\phi_0))^{L+1/2}}+\frac{(1-\gamma^2)^L}{2\pi}{}_2F_1(L,1;1/2;\gamma^2\cos^2(\phi-\phi_0)) \tag{3.11}$$

The most important parameter for the error evaluation is the standard deviation σ, in this case referred to the phase. Applying the definition of variance

$$\sigma^2_{\phi_{i,j}}=\int_{-\pi}^{\pi}\left|\phi_{i,j}-E\left[\phi_{i,j}\right]\right|^2 p(\phi_{i,j})d\phi_{i,j}=\int_{-\pi}^{\pi}\left|\phi_{i,j}-\phi_0\right|^2 p(\phi_{i,j})d\phi_{i,j} \tag{3.12}$$

that can be explicitly evaluated distinguishing two possible cases, based on the type of the target, point or distributed. The differences between them are briefly presented in the next section, where it is possible to observe how the magnitude $|\gamma|$ of the coherence can be interpreted as an indicator of the phase variance, leading to small correlation (higher decorrelation and lower quality) for low values and greater correlation (higher quality) for high coherence, $|\gamma|\approx 1$. As it has been shown in this section, the phase statistics are fully characterized by the coherence γ.

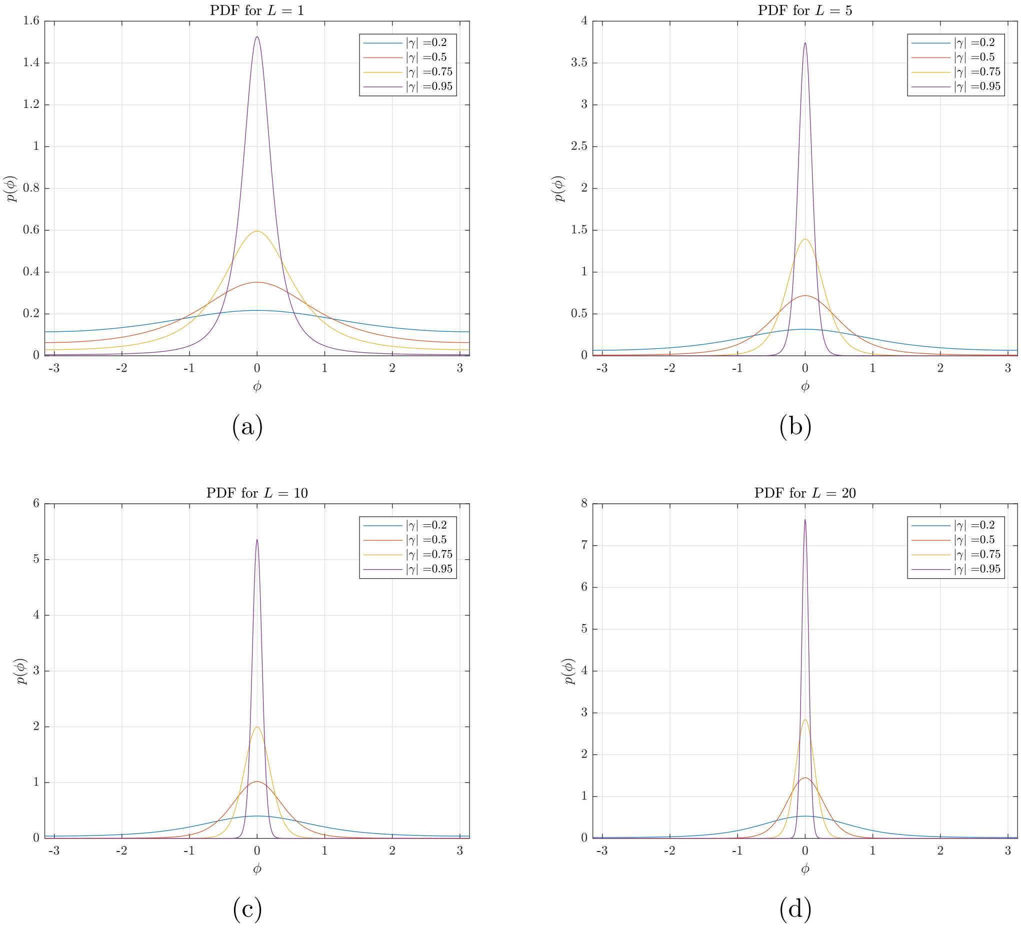

Figure 3.5: Phase distribution versus coherence $|\gamma|$ for different effective multilook factors: $L = 1$ (a), 5 (b), 10 (c), 20 (d).

3.1.2 Phase quality estimators

SAR targets can be classified as point scatterers or distributed scatters. The discrimination is done based on their reflecting properties as well as on their dimensions with respect to the size of the resolution cells of the system.

Point Scatterers Point scatterers are deterministic scatterers, i.e., objects whose electromagnetic characteristics do not vary over time, whose response dominates a resolution cell and doesn't change significantly with different acquisition geometries. Their response can be usually considered as deterministic and the coherence $|\gamma|$ values remain close to 1 across all the interferograms. For point scatterers and no multilook ($L = 1$), the phase variance can be computed as

$$\sigma^2_{\phi_{i,j}} = \frac{1 - \gamma^2}{2\gamma^2}[\text{rad}^2] \tag{3.13}$$

Distributed Scatterers Distributed Scatterers are set of targets with same backscattering properties whose response, although being characterized by a lower power than the one of the deterministic ones, can be considered coherent in space when averaged. The expectation values in (3.7) are then substituted by empirical averaging over a set of L neighbours pixels, leading to the Maximum Likelihood Estimator:

$$\hat{\gamma} = \frac{\sum_{k=0}^{L-1} S_i(k) S_j(k)^*}{\sqrt{\sum_{k=0}^{L-1} |S_i(k)|^2 \sum_{k=0}^{L-1} |S_j(k)|^2}} \tag{3.14}$$

that is biased for low coherence values. The estimated value can then be used to computed the phase variance providing a quality measurement for each pixel of the interferogram at the price of a reduction in resolution proportional to L. The estimated phase standard deviationa for different values of coherence and multilook is represented in fig. 3.6.

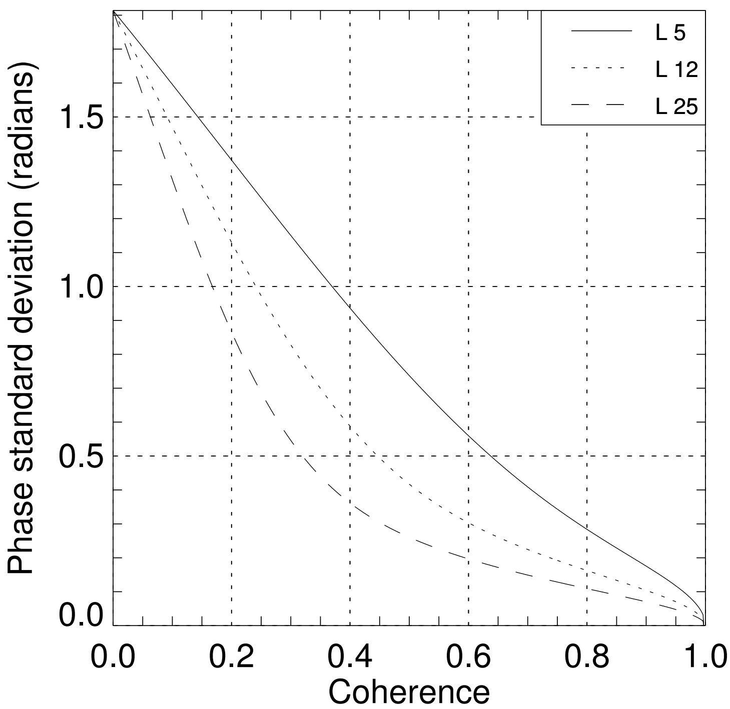

Figure 3.6: Estimated phase variance for point scatterers for different values of L [10].

3.2 Stochastic sources of errors

Decorrelation effects affect the interferometric phase introducing additional terms that are usually considered as noise or errors with respect to the quantities that are to be extracted. This noise affects the phase only if its decorrelation length is smaller than then the estimation window length, i.e. they compromise the averaging in eq. (3.14).

Following from the considerations of the previous section, the variance of the phase and therefore these effects can be studied also in terms of coherence. As just mentioned, errors with large correlation lengths, like orbital errors and atmospheric artifacts do not have impact on the coherence. In particular, the former can be almost completely removed thanks to the high precision in the positioning information of the satellite. The latter are due to the effects of the atmosphere crossed by the radar pulse. The typical decorrelation length of the atmospheric artifacts is generally around 1 km.

Several small decorrelation errors degrade the coherence magnitude:

$$|\gamma| = \gamma_{reg}\gamma_{geom}\gamma_{fdc}\gamma_{vol}\gamma_t\gamma_{th} \tag{3.15}$$

where clearly the absolute value of each term is lower than 1 and contributes to decreasing the overall coherence.

The processing-induced decorrelation γ_{reg} is due to the corregistration errors. If the corregistration reaches an accuracy of more than 1/16 the dimension, this term can be neglected.

γ_{geom} is the geometric decorrelation caused by the different incident angles of the two acquisition composing the interferogram. It can be reduced by filtering the SLCs before the interferograms generation, sacrificing resolution.

The Doppler centroid decorrelation factor γ_{fdc} is caused by the differences in the Doppler centroids of the two acquisitions.

The volumetric decorrelationγ_{vol} depends on the penetration of the radar wave into the target. It strongly depends on the distribution of the heights of the targets in a resolution cell.

γ_t is the temporal decorrelation, that accounts for the changes in the targets in the time between the two acquisitions.

γ_{th} is the thermal noise introduced by the system, for instance by the antenna.

A complete characterization on all the decorrelation effects is given in [3]. A mathematical model including all the above contributions and their effect on the phase will be presented in the chapter chapter 5, when dealing with the specific case of the output of the CPT.

Chapter 4

CPT processing

This chapter analyses in depth the CPT agorithm. The ideas presented in chapter 2 are developed in this context, offering a brief explanation of the mathematical bases that are behind each step. This is particularly important for the understanding of next chapter, that analyses the propagation of the error from the interferometric phase to the results through each passage.

Note that, as mentioned above, only PSI processing is considered. Therefore, it is assumed that a correct generation of the interferograms can provide the data needed at the input of the algorithm.

4.1 Overview

The objective of this algorithm is to provide an estimation of the line of sight (LOS) velocity of the targets and of the DEM error in the geographical areas contained in the considered stack of interferograms.

Several kinds of target motions can be observed according to different aspects.

- Based on the speed, there may be abrupt ground deformations that deeply change the topography of a region in the matter of minutes, e.g. in case of violent earthquakes, sudden vulcano eruptions and landslides, or slower movements that gradually modify the area during several years. Between these two extremes, a wide range of phenomena can be detected, for instance medium-velocity human activities such as construction works. The speed can in turn have linear and non-linear components, that, as it will become clear in the following, require different techniques.

- Based on the motion direction, the priviledged direction is the vertical one. It is possible to distinguish between upward and downward movement, the latter called uplift and the latter subsidence.

The CPT receives as input a stack of I interferograms and produces as outputs an estimation of the target velocity and of the DEM error on a selected area contained in the considered region. A third output is the azimuth position, but it has not been considered for this work.

This section of the algorithm is in turn divided in a linear and non-linear part, being devoted respectively to the estimation of a linear model for the whole stack and to the retrieval of the residual non-linear displacement components.

4.2 Linear Estimation

In this section the working principles of the linear block of the CPT algorithm are illustrated. Fig. 4.1 reports the general flowchart for this part.
The first step of the linear estimation is the pixel selection, through which only the high quality pixels are selected and passed to the following steps. Different quality metrics can be chosen, all aimed to guarantee a high phase stability. A Delaunay triangulation is then performed on the selected pixels, establishing relations or links between neighbour nodes. The linear model is thus derived for the links rather than on the single pixels, exploiting the several advantages described in section 4.2.3. This is a linear regression model, where the unknown parameters are the linear velocity v, the DEM error ϵ and the azimuth position term ξ.

Although the deformation pattern can be quite complex, in case of subsidence or uplift the main component of the velocity v can be considered linear.

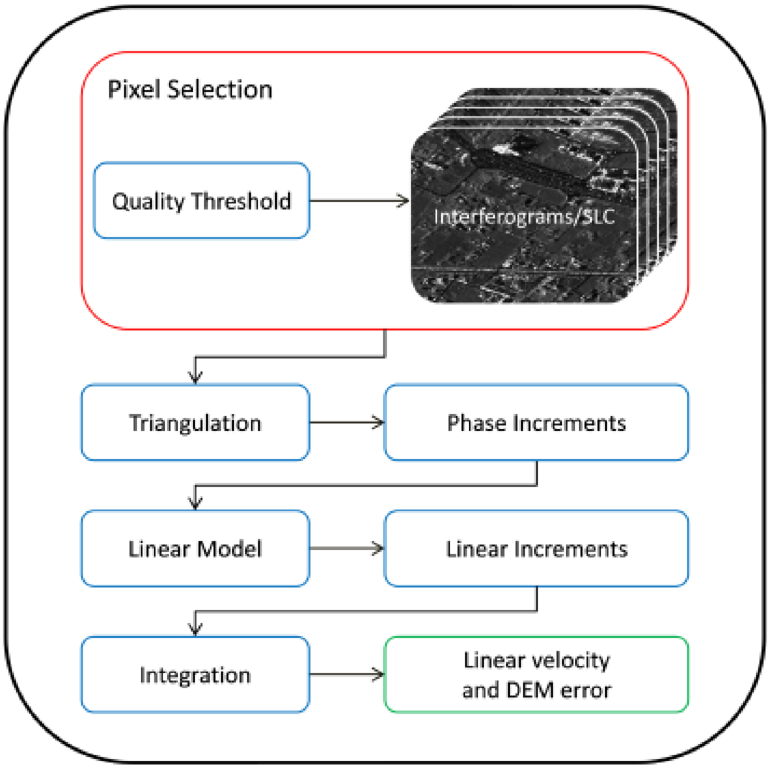

Figure 4.1: Flowchart for the linear estimation block [10].

The DEM error is, as the name suggests, due to errors in the external DEM used in the processing to remove the topographical phase term. This is especially true in urban areas, where the environment is more dynamic than in rural areas.
The azimuth position term is related to the presence of point scatterers that may not be sampled, in the SLC image, at the peak of their response, introducing a phase term proportional to the Doppler centroid. In this work only images with low Doppler differences are considered, making this term negligible.

The linear velocity and DEM error are finally obtained for each pixel from the link parameters through an integration process.

4.2.1 Pixel Selection

Coherence As explained in chapter 3, the complex coherence γ is directly related to the standard deviation σ_ϕ of the interferometric phase ϕ. Therefore, coherence can be used as an useful indicator of the phase quality. Based on this, pixels can be selected using either an "on-off" threshold, discarding the ones with an average coherence over the interferogram stack lower than the desired level, or keeping only the ones whose coherence remains above a threshold for a certain percentage of interferograms. In order to obtain a good coherence estimation, that requires an empirical average over patches of pixels with the same backscattering

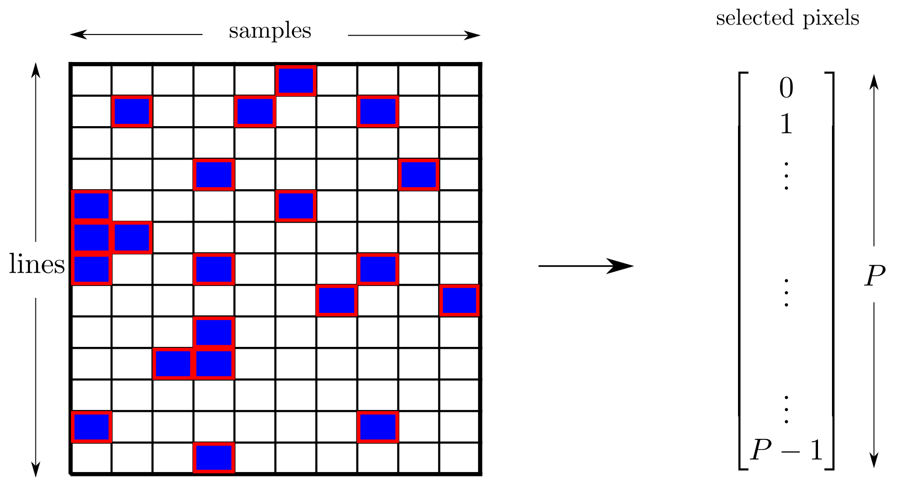

Figure 4.2: The P pixels that satisfy the selection requirements are numbered in an ordered vector.

properties, this technique is preferable in presence of distributed scatterers (see Section 3.1.2). Commonly, standard deviation up to 20° is tolerated.

Amplitude Dispersion For high SNR values, a low amplitude dispersion of the backscattered signal is correlated to a low phase standard deviation of the same. For a target whose amplitude changes according to a distribution having mean m_A and standard deviation σ_A, the amplitude dispersion is quantified as

$$D_A = \frac{\sigma_A}{m_A} \tag{4.1}$$

The two quantities D_A and σ_ϕ are related as shown in Fig 4.3. The error bars decrease when the number of SLC increases, making this method suitable only if a large number of images.

The relation holds only for high SNR targets, making it indicated for deterministic targets. This is the case for point scatterers and strong reflectors, such as man-made structures that are stable in time. Notice that these properties may be strongly dependent on the acquisition geometry, i.e., they may vary with even slight changes of the incident angle., meaning that the correspondent pixel wouldn't be selected by this method. The amplitude dispersion can work with full resolution images, providing an estimate of the phase standard deviation at the SLC level.

In this work, the coherence selection method is preferred over the amplitude dispersion one. In the following, the symbol for each of the P selected pixels is p.

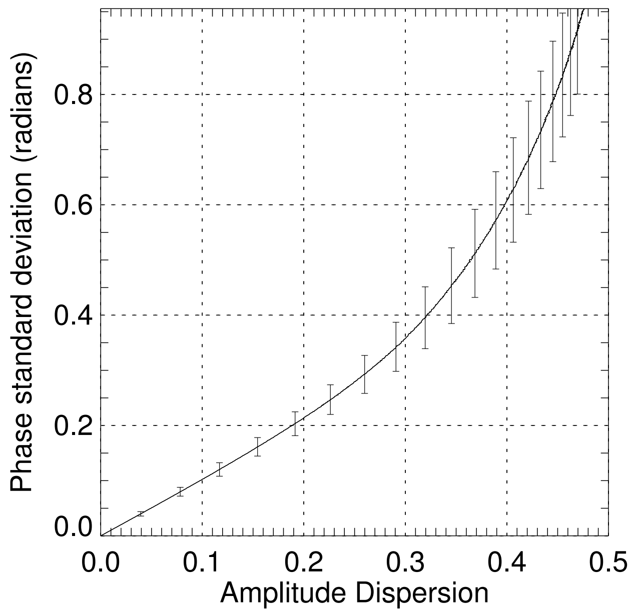

Figure 4.3: Relation between the amplitude disperion D_A and the phase standard deviation σ_A

4.2.2 Linear Model

To understand the importance of the triangulation between the pixels, it is first necessary to introduce the linear model that is used to fit the linear components of the phase that are common to all the interferograms of the stack. The linear equation is [10]

$$\phi_{lin}(p) = k_{T_i} v(p) + k_{B_i} \epsilon(p) - 2\pi k_{f_{dc}} \xi(p) \tag{4.2}$$

where k_{T_i}, k_{B_i} and $k_{f_{dc}}$ are constants related to the geometry of the system that allow the conversion from meters to radiants. In particular:

- $k_{T_i} = \frac{4\pi}{\lambda} T_i$ is the linear velocity constant, that depends on the temporal baseline T_i of the i-th interferogram;
- $k_{B_i} = \frac{4\pi}{\pi} \frac{B_i}{r_0 \sin(\theta_i)}$ is the DEM error constant, determined by the spatial baseline B_i, the incidence angle θ_i and the distance of the satellite r_0;
- $k_{fdc} = \frac{f_{dc_S}}{v_S} - \frac{f_{dc_M}}{v_M}$ is the azimuth position constant, obtained from the Doppler difference between the slave and master image and the velocity of the satellite at the respective acquisition times, v_S and v_M respectively. As already mentioned, the azimuth position is relevant only for high Doppler differences, that may be the case for ERS-Envisat datasets. In this work, from now on this term is considered negligible.

Note that in (4.2) the model is adjusted to all interferograms on a pixel level, i.e., for each pixel p of the selected ones.

Each interferogram of the stack may present an unknown random phase offset as well as be affected by random noise caused by turbolent atmospheric effects [10]. These contributions make the direct estimation of the linear components extremely difficult, undermining the reliability of the results.
An effective way to cancel the phase offset is applying a pixel triangulation. The triangulation creates a network connecting the pixels through oriented links; instead of directly estimating the linear parameters, the increments over each link are computed. By computing the difference, the phase offset of each node cancels out. The cost for this operation is dual: on one side the creation of the graph, that is of fundamental importance in order to obtain good resuts; on the other, the adjustment of the model is performed on the increments, therefore the linear parameters has to be obtained through an integration process at the end of the algorithm.

4.2.3 Triangulation and linear increment model

Several methods are available to perfom pixel triangulation. In this work the chosen technique is the Delaunay triangulation, that creates the links so that no node is inside the circumcircle of any of the created triangles. The result of the triangulation is a network of L links, each denoted with l, interconnecting the set of P pixels p. A detailed mathematical analysis of this technique is out of the scope of this work. Nevertheless, it is important to stress again the fundamental role played by the graph. As it should be clear from the previous considerations, an effective triangulation must be densely connected. Increments between isolated pixels are subject to errors: on one hand, the more the links connected to one pixel, the higher the number of equations that constrain the solution. On the other hand, a pixel connected to few others may indicate that the links are stretched through great distances. This, on turn, may compromise the "locally isotropic" hypothesis mentioned in the previous section: if the phase offset is not perfectly uniform, but slowly varies with the position of the pixel, the phase increments over long links do not cancel it out, making the triangulation ineffective.

The model for the linear increments is easily derived from eq. (4.2):

$$\Delta\phi_{lin}(l) = k_{T_i}\Delta v(l) + k_{B_i}\Delta\epsilon(l) \tag{4.3}$$

where it can be noticed that the linear quantities have been substituted by the corresponding increment and the model is now defined for each link l rather than on a pixel basis.

The linear velocity and DEM error increment $\Delta v(l)$ and $\Delta\epsilon(l)$ are obtained minimizing a quadratic cost function, called Model Adjustment Function, that is defined on each link l as

$$\Gamma(l) = \sum_{i=1}^{I} \left| e^{-j\Delta\phi_i(l)} - e^{-j\Delta\phi_{lin,i}(l)} \right|^2 \tag{4.4}$$

The minimization provides as outputs the pair $\Delta v(l), \Delta\epsilon(l)$ that minimizes the cost function in eq. 4.4.

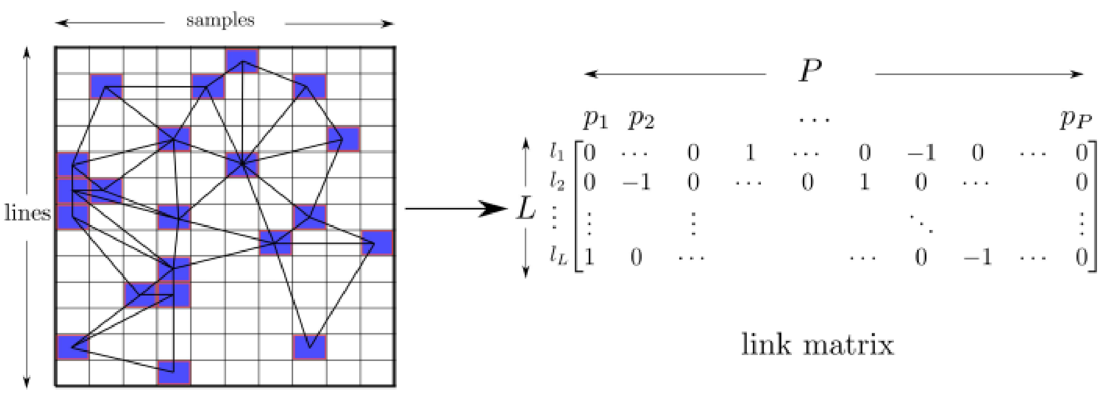

Figure 4.4: The triangulation establishes L links between the selected pixels. Matrix A contains the relations between pairs of pixels.

4.2.4 Integration

The last step of the linear estimation is the integration, that allows the retrieval of the linear values of velocity $v(p)$ and DEM error $\epsilon(p)$ for each pixel p. Each link l connects two pixels; all the links can be collected in a "connection matrix" A of dimensions $L \times P$, where each row corresponds to a link and contains -1 or $+1$ on the columns associated to the pixels that the link connects. The different sign implicitly identifies the orientation of the link.

The integration is performed solving the linear system that from the increments x determines the linear values y:

$$\mathbf{y} = \mathbf{A}\mathbf{x} \tag{4.5}$$

For how it is defined, the system has infinite solutions that differ by an offset. The solution is therefore called "floating" and needs a point, called seed, of known velocity or DEM error to be fixed. In this way, due to the differential nature of the system, the output parameters are referred to the values of the seed.

4.3 Non-Linear Estimation

The linear estimation provides only the main component of the target velocity. A new estimation is required to correctly identify the non-linear components of the displacements. The error propagation for this block of the CPT technique has not been studied, therefore only a brief overview is offered.

After the linear estimation, the estimated linear components have to be removed from the interferometric phase. The residual phase is then

$$\phi_{res} = \phi - k_T v - k_B \epsilon \tag{4.6}$$

and it accounts for the non-linear components, that cannot be modelled by a linear estimator (more on this problem in the following chapter). Two main contributions can be identified in the residual phase: atmospheric artifacts and non-linear displacement. A third one would be the residual phase cycles due to highly non-linear patterns. According to this considerations, the non-linear block of the CPT is divided in two steps:

- unwrapping of the phase and estimation of atmospheric artifacts;
- estimation of the non-linear displacement.

The phase expression can be rewritten, after the application of a low-pass spatial filter to reduce the effects of the non-linear deformation, as

$$\phi_{res,filt} = \phi_{NL,res} + \phi_{atm} \tag{4.7}$$

Based on this decomposition, the non-linear processing estimates the Atmospheric Phase Screen (APS) as well as the non-linear displacement term.

The non-linear block is not further investigated in this work, as the focus is mainly on the propagation of the error through the linear one. A general scheme is included for completeness in Fig. 4.5.

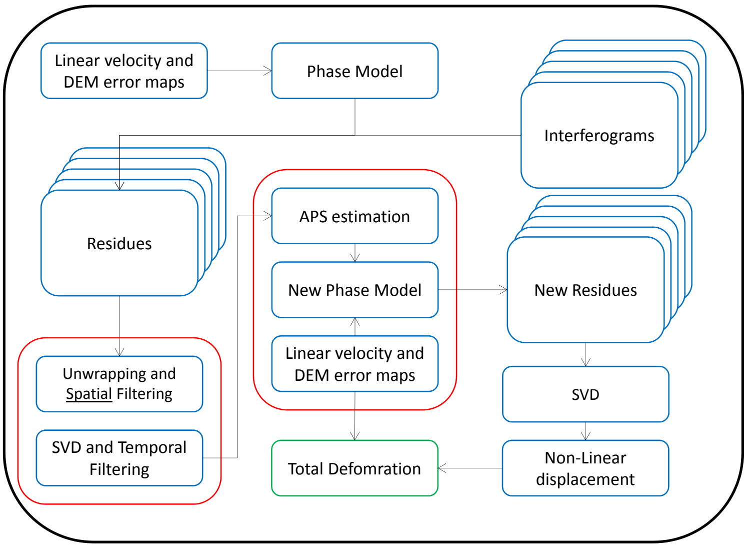

Figure 4.5: Flowchart for the non linear estimation block [10].

Chapter 5

Error propagation in DInSAR Processing

This chapter contains the core of this work. First, a brief introduction presents the general theory of the error propagation through different kinds of mathematical manipulations. In the second section this theoretical framework is applied to the case of interest, i.e., from the phase (measured data) to the velocity and DEM error (outputs). A more in-depth explanation on the IDL implementation can be found in Appendix A.

5.1 General Theory of Error Propagation

The uncertainty in any kind of measurement is usually expressed through the standard deviation σ of the distribution of the acquisitions. In the specific case of interest, the measures on the phase are affected by the random processes, considered overall as noise, described in chapter 3. This section provides the mathematical tools for propagating the initial uncertainty on the interferometric phase to the output of the CPT algorithm. The expressions are always provided in terms of variance, from which the standard deviation can be immediately retrieved. The relation between the input and output covariance matrices are derived for all the functions that are used in the CPT: linear transformation (from the nodes to the links of the triangulation), minimization and linearization (from the phase increments to the linear increments) and finally integration.

Linear transformation of a random vector Starting from the very basic concepts, consider a N-dimensional random vector $\mathbf{x}$ characterized by the corresponding $N \times N$ covariance matrix $\mathbf{\Sigma}_x$. The diagonal values represent the variance of each component and the off-diagonal ones the covariance between pairs of different components. Solving the linear system $\mathbf{y} = \mathbf{A}\mathbf{x}$ determined by the $M \times N$ matrix $\mathbf{A}$ corresponds to performing a linear transformation on $\mathbf{x}$. It is easy to prove that the covariance of $\mathbf{y}$ is then

$$\mathbf{\Sigma}_y = \mathbf{A}\mathbf{\Sigma}_x\mathbf{A}^T \tag{5.1}$$

On the contrary, $\mathbf{\Sigma}_x$ can be estimated from $\mathbf{A}\mathbf{\Sigma}_y$ as

$$\mathbf{\Sigma}_x = (\mathbf{A})^{-1}\Sigma_y(\mathbf{A}^T)^{-1} \tag{5.2}$$

As in general $N \neq M$, i.e. matrix $\mathbf{A}$ is not square, the pseudo-inverse $(\mathbf{A}^T\mathbf{A})^{-1}\mathbf{A}^T$ is used:

$$\mathbf{\Sigma}_x = ((\mathbf{A}^T\mathbf{A})^{-1}\mathbf{A}^T)\Sigma_y((\mathbf{A}^T\mathbf{A})^{-1}\mathbf{A}^T)^T \tag{5.3}$$

Minimization In this work, the minimization is necessary to estimate the parameters in a non linear estimation scenario. The problem can be stated as follows: the model is defined as

$$y = f(\phi_1, \phi_2, \cdots, \phi_n; \Delta_1, \Delta_2, \cdots, \Delta_L, \Delta_{L+1}, \cdots, \Delta_{2L}) \tag{5.4}$$

where the symbols for the input data ϕ_i and the parameters to be estimated Δ_i have been chosen to resemble the ones used in this specific application. In the following, the input data and the parameters will be collected for convenience in two vectors, $\boldsymbol{\phi}$ and $\mathbf{\Delta}$ respectively. According to [9] and [10], a possible approach is to linearize the non linear function through its Taylor approximation. In particular, the Taylor expansion is computed around zero, that is the case for the specific application of interest, as pointed out in the next section.

Firstly, recall that the cost function is $\Gamma(l)$ as defined in eq. (4.4). In this section, a more appropriate notation would be $\Gamma(\boldsymbol{\Delta})$ to highlight that the minimization is performed with respect to the parameters to be estimated, i.e. the problem is stated as

$$\hat{\boldsymbol{\Delta}} = \arg\min_{\boldsymbol{\Delta}} \left[\Gamma(\boldsymbol{\Delta})\right] \tag{5.5}$$

Secondly, the Jacobian matrix of $f(\cdot)$ is defined as the $n \times 2L$ matrix

$$\mathbf{J} = \begin{bmatrix} j_{1,1} & \cdots & j_{1,2L} \\ \vdots & \ddots & \cdots \\ J_{n,1} & \cdots & j_{n,2L} \end{bmatrix} \tag{5.6}$$

with each column can be computed as

$$j_i = \frac{\partial f(\phi_1, \phi_2, \cdots, \phi_n; \Delta_1, \Delta_2, \cdots, \Delta_L, \Delta_{L+1}, \cdots, \Delta_{2L})}{\partial \Delta_i} \tag{5.7}$$

In this scenario, the solution of the Least Square minimization of the non linear function is approximated as

$$\hat{\boldsymbol{\Delta}} = \left(\mathbf{J}^T\mathbf{J}\right)^{-1}\mathbf{J}^T\mathbf{y} \tag{5.8}$$

and the corresponding variance is computed as in eq. (5.3)

$$\boldsymbol{\Sigma}_\Delta = \left(\left(\mathbf{J}^T\mathbf{J}\right)^{-1}\mathbf{J}^T\right)\boldsymbol{\Sigma}_y\left(\left(\mathbf{J}^T\mathbf{J}\right)^{-1}\mathbf{J}^T\right)^T \tag{5.9}$$

The validity of the approximations is briefly discussed in section 5.2.3.

5.2 Linear Estimation

As seen in the previous section, the parameter that is used to describe the error on a measured quantity is its standard deviation, or, equivalently, its variance. In this section the general concepts illustrated above are applied to the specific case of the CPT estimation of the linear velocity and of the DEM error.

The first section will analyse the construction of the initial covariance matrix, i.e., the covariance matrix of the phase.

The following sections will propagate the original uncertainty through the various steps of the CPT algorithm as they were presented in chapter 4. At each step, the output covariance matrix is derived from the input one. Following the data flow, the error is propagated trough the triangulation, where the covariance of the increments is computed. The same is done for the linear model minimization and finally for the linear quantities is computed.

The implementation details are kept to the minimum. Due to the really huge size of the processed data and of the processing matrices, a carefully optimized code is required. As it may be interesting and useful for future applications, in appendix A some more technical observations are reported.

5.2.1 Interferometric Phase Covariance Matrix

The uncertainty on the interferometric phase ϕ is represented by its covariance matrix $\mathbf{\Sigma}_{\phi}$, that accounts for the overall effect of three major factors:

- the APS noise. The unpredictable phase delay due to propagation of the radio waves through the atmosphere is one of the main sources of noise [11].
- the decorrelation effects. As explained in chapter 3, continuous changes in the observed area and several other phenomena such as geometric factors contribute to the decorrelation of the images in the time dimension, i.e., across the interferogram stack.
- the thermal noise. As mentioned in chapter 3, the various thermal contributions degrade the phase quality.

The effect of each of these elements can be taken into account by a corresponding covariance matrix: $\mathbf{\Sigma}_{\phi_{APS}}$ for the atmospheric artifact covariance and $\mathbf{\Sigma}_{\phi_{decorr}}$ for both the decorrelation and thermal noise, whose contribution is estimated in the same way. Under the well-verified hypothesis of independence between the three, the overall covariance matrix for the i-th interferogram is the $P \times P$ matrix

$$\mathbf{\Sigma}_{\phi} = \mathbf{\Sigma}_{\phi_{APS}} + \mathbf{\Sigma}_{\phi_{decorr}} \tag{5.10}$$

In the remaining of this section, the structure and the properties of the three individual covariance matrices are briefly analysed.

APS covariance Atmospheric effects present a high variability, i.e., their contribution to the phase ranges from being negligible to dominating the phase [11]. Therefore, it is important to be able to identify and model them for assessing the realiability of the results on the deformation patterns. These unpredictable effects can be well represented by a stochastic model. Usually, the APS is assumed to be isotropic; in [13] an in-depth analysis has been carried out and an advanced model for the estimation of the APS variance under anisotropic assumption has been proposed. For simplicity, in this work the APS is considered isotropic, but the extension to the anisotropic case is immediate.

As in general the atmosphere can be considered a random process uncorrelated in time and correlated in space with a correlation length of around 1 km, its variance can be computed using an empirical semivariogram. For a random function (RF) $\eta(\mathbf{s})$ defined over an image $\mathbf{S} = \{(x, y)\}$, the variogram $2\gamma(\mathbf{s}_i, \mathbf{s}_j)$ is defined as the variance of the difference $\Delta\eta(\mathbf{s}_i; \mathbf{s}_j)$ between the values of the random process at two different locations $\mathbf{s}_i = (x_i, y_i), \mathbf{s}_j = (x_j, y_j)$:

$$2\gamma(\mathbf{s}_i; \mathbf{s}_j) = \mathrm{Var}\left[\Delta\eta(\mathbf{s}_i; \mathbf{s}_j)\right] = \mathrm{Var}\left[\eta(\mathbf{s}_j) - \eta(\mathbf{s}_i)\right] = \tag{5.11}$$

$$= \mathrm{E}\left[\left(\eta(\mathbf{s}_j) - \eta(\mathbf{s}_i) - \mathrm{E}\left[\eta(\mathbf{s}_j) - \eta(\mathbf{s}_i)\right]\right)^2\right] \tag{5.12}$$

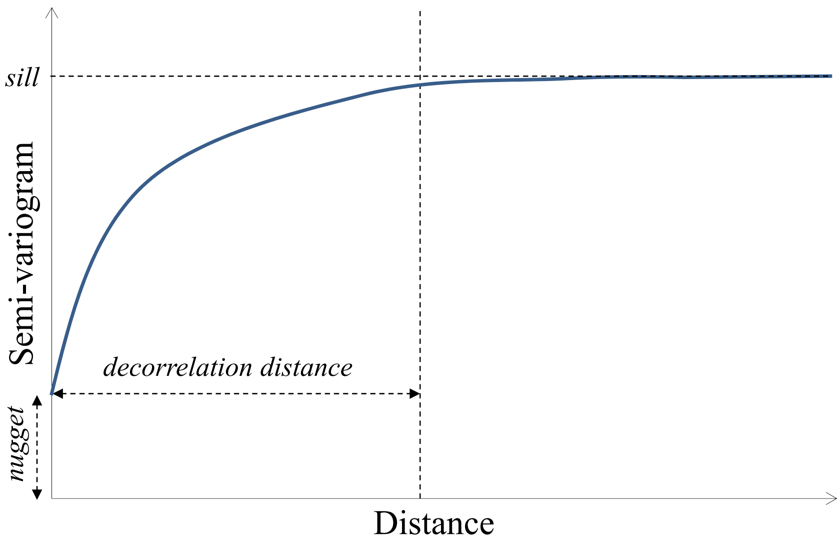

Figure 5.1: Ideal variogram behaviour and related parameters [10].

The semivariogram is simply computed as half of the variogram. The different name and usage is simply due to notational convenience.

If the process is stationary, the variogam is a function only of the difference between the pixel positions:

$$2\gamma(\mathbf{s}_i; \mathbf{s}_j) = 2\gamma(\mathbf{s}_i - \mathbf{s}_j) \tag{5.13}$$

For an isotropic stationary process, the variogram can be expressed as a function of the distance h between two points $\mathbf{s}_i, \mathbf{s}_j$:

$$\begin{aligned} &2\gamma(\mathbf{s}_i; \mathbf{s}_j) = 2\gamma(h) \\ &\qquad \forall \mathbf{s}_i, \mathbf{s}_j \text{ s.t. } ||\mathbf{s}_i - \mathbf{s}_j|| = \sqrt{(x_i - x_j)^2 - (y_i - y_j)^2} = h \end{aligned} \tag{5.14}$$

An ideal theoretical variogram presents the trend depicted in fig. 5.1 and can be described using three parameters [12]:

- the sill $\sigma_S^2 = \lim_{h\to\infty} 2\gamma(h)$ is the limiting value of the variogram for infinite distance;
- the nugget n is the height of the jump of the semivariogram at the discontinuity at the origin;
- the range r is the distance in which the difference of the variogram from the sill becomes negligible.

Recall that the objective is to obtain a reliable estimation of the APS standard deviation; more specifically, the matrix $\mathbf{\Sigma}_{\phi_{APS}}$ has to be filled with the atmospheric

variance values $\sigma^2_{\phi_{APS}}$ along the diagonal and with the corresponding values of covariance $\sigma^2_{\phi_{APS}}(p_i, p_j)$ between pixels (p_i, p_j) in the off-diagonal positions.
The relation between the variogram and the variance can be easily computed considering the definition of the former as given in (5.12):

$$\begin{aligned} 2\gamma(h) &= \mathrm{E}\left[(\Delta\eta(\mathbf{s}_j;\mathbf{s}_i) - \mathrm{E}\left[\Delta\eta(\mathbf{s}_j;\mathbf{s}_i)\right])^2\right] = \\ &= \mathrm{E}\left[\eta^2(\mathbf{s}_i)\right] + \mathrm{E}\left[\eta^2(\mathbf{s}_j)\right] - 2\mathrm{E}\left[\eta(\mathbf{s}_j)\eta(\mathbf{s}_i)\right] \end{aligned} \tag{5.15}$$

Note that this holds under the isotropic, stationary and homogeneous hypotheses that guarantee that $\mathrm{E}\left[\eta(\mathbf{s}_j)\right] = \mathrm{E}\left[\eta(\mathbf{s}_i)\right] = \mu_\eta$ for all the interferogram pixels. This also allows to rewrite again eq. (5.15) as

$$\gamma(h) = \mathrm{Var}\left[\eta(\mathbf{s})\right] - \mathrm{Covar}\left[\eta_h\right] \tag{5.16}$$

that is the fundamental equation that under the above assumptions relates the variogram to the variance and covariance. The symbol $\mathrm{Covar}\left[\eta_h\right]$ indicates the covariance between two general pixels at distance h.
From eq. (5.16) the variance of each pixel p can be computed as

$$\sigma^2_{\phi_{APS}}(p) = \sigma^2_S = \lim_{h\to\infty} 2\gamma(h) \tag{5.17}$$

exploiting the fact that pixels at infinite lag distance are decorrelated. In other words, the sill of the variogram represents the variance for all the pixels of the considered interferogram. It is important to explicitly underline that using this estimation the pixel variance is estimated at an interferogram level, and thus has the same value for all the pixels in the same interferogram.

More critical is the covariance, that needs to be computed for each pair (p_i, p_j) of selected pixels considering the distance h between them and the associated variogram value. Under the conditions stated above, the covariance is a function only of the distance h between pairs of pixels and is obtained from the variogram as:

$$\sigma^2_{\phi_{APS}}(h) = \sigma^2_{\phi_{APS}}(p_i, p_j) = \sigma^2_S - 2\gamma(h) \tag{5.18}$$

Eq. (5.18) requires the construction of a distance network between all the possible pairs of the P selected pixels.

Note that the expression of the variogram in (5.14) requires the computation of an expected value, that in turns is computed over an infinite number of realizations. Therefore in practice an empirical variogram is used instead of the ideal one. The empirical variogram is an estimate of the theoretical semivariogram and measures the spatial variability of a regionalized variable, or in other words, it describes dissimilarity of values at points with distance h [13]. In the empirical variogram, distances are substituted by distance bins. Each bin b_i has radius δ and center h_i and contains all the distances h such that $|h - h_i| \le \delta$. Pratically, the distance between all possible pairs of pixels is computed and a corresponding histogram is built. From it, the empirical variogram for two pixels i, j at distance h can be expressed as:

$$2\gamma(h) = \frac{1}{N_h} \sum_{i,j \in h} (\eta(\mathbf{s}_j) - \eta(\mathbf{s}_i))^2 \tag{5.19}$$

being N_h the number of pairs of pixels in the bin that contains distance h.
The correct estimation of the variograms and consequently of the variance of random fields has been extensevely studied in [14] and in [13] for the APS covariance in particular.

Once obtained the variogram for each interferogram, the distance network and the corresponding histogram, the diagonal of the APS covariance matrix is filled according to (5.17) and the remaining elements according to (5.18) and the relative distances. The final result is a dense $P \times P$ matrix, whose structure is further clarified in eq. (5.20)

$$\mathbf{\Sigma}_{\phi_{APS}} = \begin{bmatrix} \mathbf{\Sigma}_{\phi_{APS}} & \mathbf{\Sigma}_{\phi_{APS}}(1,2) & \mathbf{\Sigma}_{\phi_{APS}}(1,3) & \cdots & \mathbf{\Sigma}_{\phi_{APS}}(1,P) \\ \mathbf{\Sigma}_{\phi_{APS}}(2,1) & \mathbf{\Sigma}_{\phi_{APS}} & \mathbf{\Sigma}_{\phi_{APS}}(2,3) & \cdots & \mathbf{\Sigma}_{\phi_{APS}}(2,P) \\ \vdots & \vdots & \vdots & \vdots & \vdots \\ \mathbf{\Sigma}_{\phi_{APS}}(P,1) & \mathbf{\Sigma}_{\phi_{APS}}(P,2) & \mathbf{\Sigma}_{\phi_{APS}}(P,3) & \cdots & \mathbf{\Sigma}_{\phi_{APS}} \end{bmatrix} \tag{5.20}$$

where each element $\mathbf{\Sigma}_{\phi_{APS}}(\cdot)$ is a $I \times I$ matrix that contains the variance or covariance values for each of the I interferograms. According to the previous considerations, the diagonal elements $\mathbf{\Sigma}_{\phi_{APS}}$ are all equal whereas the off-diagonal $\mathbf{\Sigma}_{\phi_{APS}}(p, q)$ are filled with the covariance values between pixel p and q as obtained for each interferogram from the corresponding variogram according to their distance.

Decorrelation and Thermal noise Covariance Matrix As discussed in chapter 3, the quality of the interferograms is affected by various sources of decorrelation. The estimators for the phase standard deviation that have been presented provide an estimate $\sigma_\psi(p)$ for each pixel p of each SLC image. Given the estimate $\sigma^2_{\psi_M}(p)$ for the master M and $\sigma^2_{\psi_S}(p)$ for the slave S, the variance value for the corresponding interfegram i can be computed as

$$\sigma^2_{\phi_{decorr,i}}(p) = \sigma^2_{\psi_M}(p) + \sigma^2_{\psi_S}(p) \tag{5.21}$$

For the amplitude dispersion approach, each image of the set presents the same standard deviation. Therefore, all the interferograms are assumed to have equal variance

$$\sigma^2_{\phi_{decorr,i}}(p) \tag{5.22}$$

On the contrary, multilooked images provide an estimation of the standard deviation at an interferogram level.

Therefore, the decorrelation covariance matrix is a $(P \cdot I) \times (P \cdot I)$ matrix having the following structure:

$$\mathbf{\Sigma}_{\phi_{decorr}} = \begin{bmatrix} \mathbf{\Sigma}_{\phi_{decorr}}(1) & [0] & \cdots & [0] \\ [0] & \mathbf{\Sigma}_{\phi_{decorr}}(2) & \cdots & [0] \\ \vdots & \vdots & \vdots & \vdots \\ [0] & [0] & \cdots & \mathbf{\Sigma}_{\phi_{decorr}}(P) \end{bmatrix} \tag{5.23}$$

where each $\mathbf{\Sigma}_{\phi_{decorr}}(p)$ of dimension $I \times I$ represents the decorrelation of pixel p across the interferograms and can be generally considered diagonal, as all the advanced DInSAR techniques operate on a subset of pixels that are coherent through an interferogram network [10]. The diagonal structure is an approximation, due to the hypothesis that the pixels are independent across the interferogram stack. The overall $(P \cdot I) \times (P \cdot I)$ covariance matrix $\mathbf{\Sigma}_{\phi}$ is finally obtained according to (5.10) as

$$\begin{aligned} \mathbf{\Sigma}_{\phi} &= \mathbf{\Sigma}_{\phi_{APS}} + \mathbf{\Sigma}_{\phi_{decorr}} = \\ &= \begin{bmatrix} \mathbf{\Sigma}_{\phi_{decorr}}(1) + \mathbf{\Sigma}_{\phi_{APS}} & \mathbf{\Sigma}_{\phi_{APS}}(1,2) & \cdots & \mathbf{\Sigma}_{\phi_{APS}}(1,P) \\ \mathbf{\Sigma}_{\phi_{APS}}(2,1) & \mathbf{\Sigma}_{\phi_{decorr}}(2) + \mathbf{\Sigma}_{\phi_{APS}} & \cdots & \mathbf{\Sigma}_{\phi_{APS}}(2,P) \\ \vdots & \vdots & \vdots & \vdots \\ \mathbf{\Sigma}_{\phi_{APS}}(P,1) & \mathbf{\Sigma}_{\phi_{APS}}(P,2) & \cdots & \mathbf{\Sigma}_{\phi_{decorr}}(P) + \mathbf{\Sigma}_{\phi_{APS}} \end{bmatrix} \end{aligned} \tag{5.24}$$

5.2.2 Triangulation: Covariance matrix of the Phase Increments

To find the covariance matrix of the phase increments, the phase covariance values need to be related according to the links created by the selected triangulation. These are fully described by matrix A introduce in eq. (4.5), but this latter take into accounts just the links on a single interferogram. Being the network the same for each interferogram, in order to take into account the whole stack it is sufficient to perform a Kronecker product with an $I \times I$ identity matrix I_I:

$$A \otimes I_I = \begin{bmatrix} 0 & \cdots & 0 & I_I & \cdots & 0 & -I_I & 0 & \cdots & 0 \\ 0 & -I_I & 0 & \cdots & 0 & I_I & 0 & \cdots & & 0 \\ \vdots & & \vdots & & & & \ddots & & & \vdots \\ I_I & 0 & \cdots & & & \cdots & 0 & -I_I & \cdots & 0 \end{bmatrix} \tag{5.25}$$

where the above matrix is constructed following the same example structure of Fig. 4.4. The increment matrix is thus obtained, according to eq. (5.3) as

$$\mathbf{\Sigma}_{\Delta_{\phi}} = (\mathbf{A} \otimes \mathbf{I}_I)\mathbf{\Sigma}_{\phi}(\mathbf{A} \otimes \mathbf{I}_I)^T \tag{5.26}$$

5.2.3 Linear Model adjustment: Covariance matrix of the Linear Increments

The adjustment of the linear model for the phase is performed on the complex exponential phases, as in eq (4.4). The error propagation through this step is the most cumbersome, as the neither the minimization nor the involved functions are linear. The minimization for small values of increments or for an unwrapped phase can be considered a linear regression [10], as the non linearity due to the exponentials can be removed using a Taylor expansion

$$e^{-jx} = 1 + \frac{(-jx)}{1!} + \frac{(-jx)^2}{2!} + \frac{(-jx)^3}{3!} + \cdots = \sum_{n=0}^{\infty} \frac{(-jx)^n}{n!} \tag{5.27}$$

around the correct values of velocity and DEM error. Considering only the linear term, the approximation for the considered complex exponential becomes:

$$e^{-j\sigma_{\Delta_\phi}} = 1 - jk_{T_i}\sigma_{\Delta v} - jk_{B_i}\sigma_{\Delta\epsilon} \tag{5.28}$$

that implies

$$\sigma_{\Delta_\phi} = k_{T_i}\sigma_{\Delta v} + k_{B_i}\sigma_{\Delta\epsilon} \tag{5.29}$$

In [10], the linear approximation has been shown to hold well also for high noise level. As shown in the graphs in fig. 5.2, the linear model doesn't deviate significantly from the exponential one in any of the three considered cases.

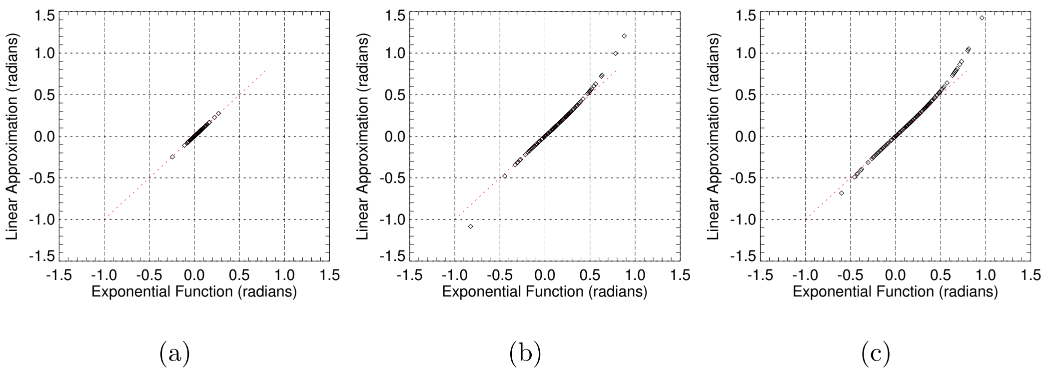

Figure 5.2: Linear approximation of an exponential around 0 for different noise levels: (a) 0.25 radians. (b) 0.8 radians. (c) 1.6 radians. [10]

The Jacobian matrix necessary for the linearization is the $I \times 2$ matrix

$$\mathbf{J}(l) = \begin{bmatrix} k_{T_1}(l) & k_{B_1}(l) \\ k_{T_2}(l) & k_{B_2}(l) \\ \vdots & \vdots \\ k_{T_I}(l) & k_{B_I}(l) \end{bmatrix} \tag{5.30}$$

that, in principle, is different for each link l as the baselines may vary with the length of the link. For practical purposes, as the considered areas are always limited, the baselines are considered constant. Thus, the Jacobian is extended to each link exploiting once again the Kronecker product: defining the $(I \cdot L) \times (2 \times L)$ matrix

$$\mathbf{G} = \mathbf{I}_L \otimes \mathbf{J} = \begin{bmatrix} \mathbf{J} & 0 & 0 & \cdots & 0 \\ 0 & \mathbf{J} & 0 & \cdots & 0 \\ \vdots & 0 & \ddots & \vdots & \vdots \\ 0 & \cdots & & & \mathbf{J} \end{bmatrix} \tag{5.31}$$

the variance at the output of the minimization step is, according to eq. (5.9)

$$\mathbf{\Sigma}_{\Delta v, \Delta \epsilon} = \left(\mathbf{G}^T\mathbf{G}\right)^{-1}\mathbf{G}^T\mathbf{\Sigma}_{\Delta\phi}\left(\left(\mathbf{G}^T\mathbf{G}\right)^{-1}\mathbf{G}^T\right)^T \tag{5.32}$$

The matrix $\mathbf{\Sigma}_{\Delta v, \Delta \epsilon}$ has dimensions $(2 \cdot L) \times (2 \cdot L)$ and it contains the covariance of the increments of the velocity v and of the DEM error ϵ. It is therefore necessary to extract the increment variance values for the two quantities, thus obtaining the $L \times L$ matrices $\mathbf{\Sigma}_{\Delta v}$ and $\mathbf{\Sigma}_{\Delta \epsilon}$. The off-diagonal elements represent the correlation between the two parameters, and in this context they are simply discarded. It would be interest, for future works, to study also its behaviour, in order to gain useful insights on the validity of some of the assumptions made throughout this work.

5.2.4 Integration: Covariance matrix of the Linear Parameters

The output covariance matrices $\mathbf{\Sigma}_v$ and $\mathbf{\Sigma}_{dem}$ are obtained from eq. (4.5) propagating the error through the linear system. Recalling what has been said in section 4.2.4, one or more pixels of known velocity and DEM error, called seeds, are needed to fix the solution. In this specific context, the seeds are necessary in order to make the connection matrix $\mathbf{A}$ non-singular and therefore invertible. The columns associated to the seeds are removed; then,

- when solving the linear system, the known values of the seeds are added or substracted to the estimated values of the connected pixels, according to the direction of the link;
- when inverting the $\mathbf{A}$ matrix, the rows associated to the links containing one seed are also removed, as the seeds, being deterministically known, have zero variance.

Naming $\mathbf{A}_{seed}$ the obtained connection matrix, $\mathbf{\Sigma}_v$ and $\mathbf{\Sigma}_{dem}$ can be derived as:

$$\mathbf{\Sigma}_v = \left(\mathbf{A}_{seed}^T\mathbf{A}_{seed}\right)^{-1}\mathbf{A}_{seed}^T\mathbf{\Sigma}_{\Delta v}\left(\left(\mathbf{A}_{seed}^T\mathbf{A}_{seed}\right)^{-1}\mathbf{A}_{seed}^T\right)^T \tag{5.33}$$

$$\mathbf{\Sigma}_\epsilon = \left(\mathbf{A}_{seed}^T\mathbf{A}_{seed}\right)^{-1}\mathbf{A}_{seed}^T\mathbf{\Sigma}_{\Delta \epsilon}\left(\left(\mathbf{A}_{seed}^T\mathbf{A}_{seed}\right)^{-1}\mathbf{A}_{seed}^T\right)^T \tag{5.34}$$

5.3 Synthetic data validation

The algorithm for the propagation of the uncertainty across the CPT has been tested on a synthetic scenario obtained using a simulator. The simulator is the same as the one used in [10] and the simulated data is briefly described in the first section. Several scenarios are tested, in order to observe different effects on the variance of the results.

Simulated data description The basic setting is described in table 5.1. The techniques utilized to perform the simulation in order to obtain the desired covariance for the atmospheric and temporal decorrelation effects, like the Monte Carlo simulation, are not described in this work.

Parameter	Value
Number of Images	51
Number of Interferograms	135
Size of the Images (pixels)	256
Multilook	3x3
Coherence Threshold	0.75
Number of Pixels	725
Maximum deformation	-2 cm/year
Maximum DEM error	10 m
Seed position (pixel coordinates)	(82,67)

Table 5.1: Synthetic scenario input data [10].

Fig. 5.3a and fig. 5.3b report respectively the velocity and the DEM error maps of the considered scenario.

The pixel selection is performed using the coherence criterion with a multilook factor of 3. The links are obtained through a Delaunay triangolation, and a maximum link distance can be set in order to tune it. The different scenarios presented in the following sections are obtained varying this parameter or applying a pixel mask to artificially hide some of the selected pixels and thus change the topology of the triangulation.
The APS covariance matrix is estimated, as explained in section 5.2.1, using the empirical variograms. In fig. 5.4b the variogram estimated from the interferogram in fig. 5.4a and the corresponding covariance matrix (5.5) are reported. It can be noted that there is a correspondance between the decorrelation distance in the variogram and the decreasing values of the covariance matrix.

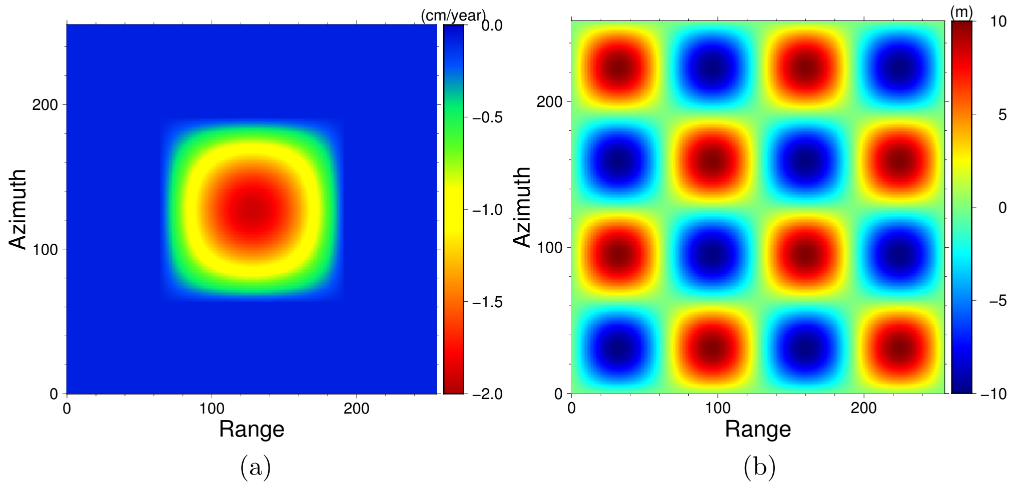

Figure 5.3: Simulated linear velocity (a) and DEM error (a).

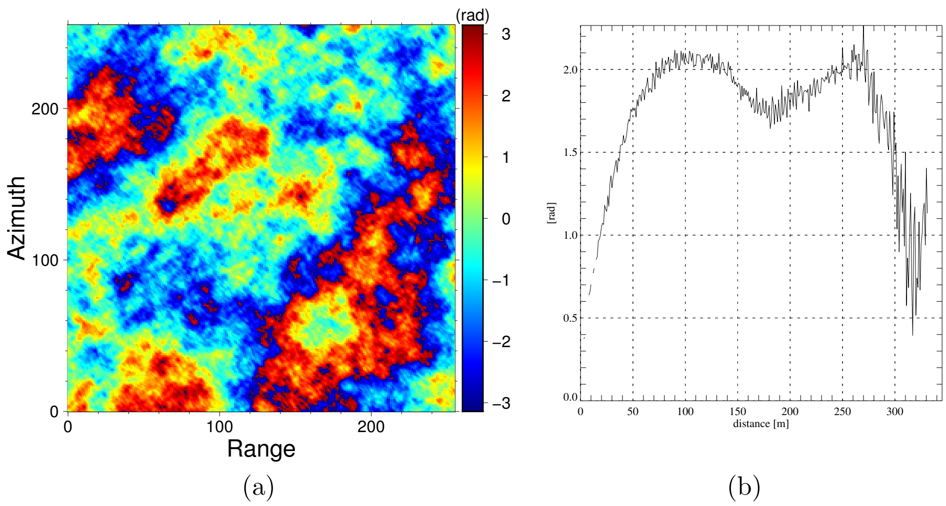

Figure 5.4: Turbolent atmospheric phase in the considered interferogram (a) and derived empirical variogram (b).

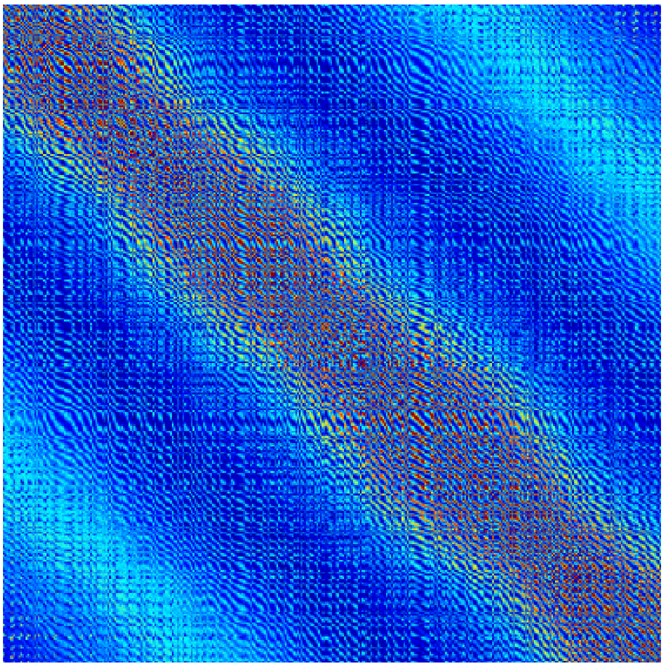

Figure 5.5: Estimated covariance matrix for the considered interferogram.

Linear Parameters estimation On a first instance, the CPT algorithm implementation of the simulator is tested. The pixel selection and the corresponding triangulation are reported in 5.6. The triangulation is initially performed under the costraint of maximum link length of 800 m. Observe that the seed is highlighted by the blue marker.

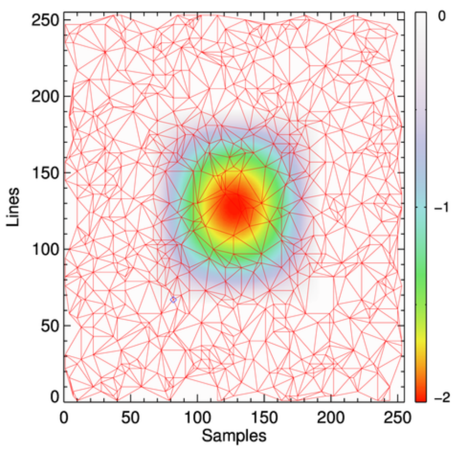

Figure 5.6: Default triangulation.

The simulated DEM error and velocity, that will be referred to as "real" values from now on, are sampled according to the pixel selection in 5.7a and 5.7b.
The estimated DEM error and linear velocity are reported in fig. 5.8a and 5.8b

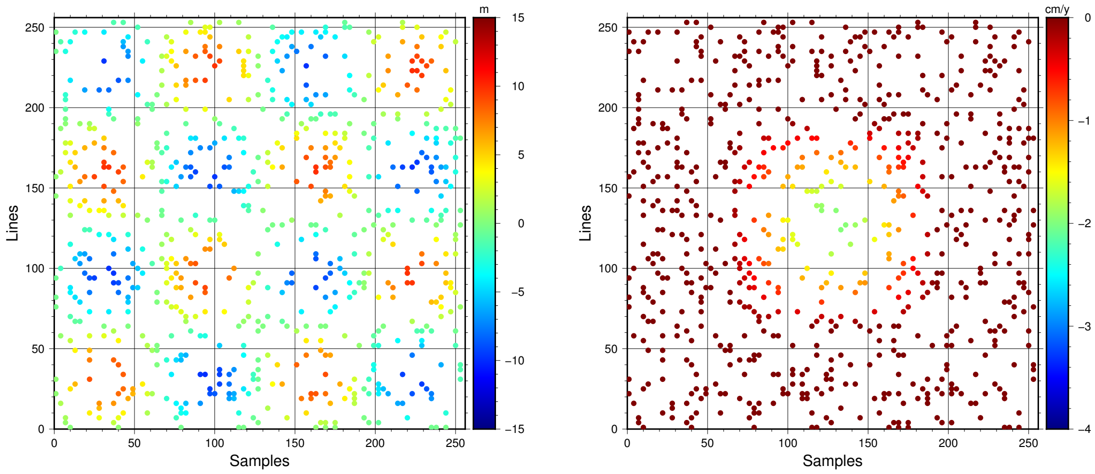

(a) (b)

Figure 5.7: Simulated DEM error (a) and linear velocity (b) sampled at the selected pixels locations.

respectively. The pattern of the estimated data corresponds to the simulated one, although it presents some errors in the amplitude.

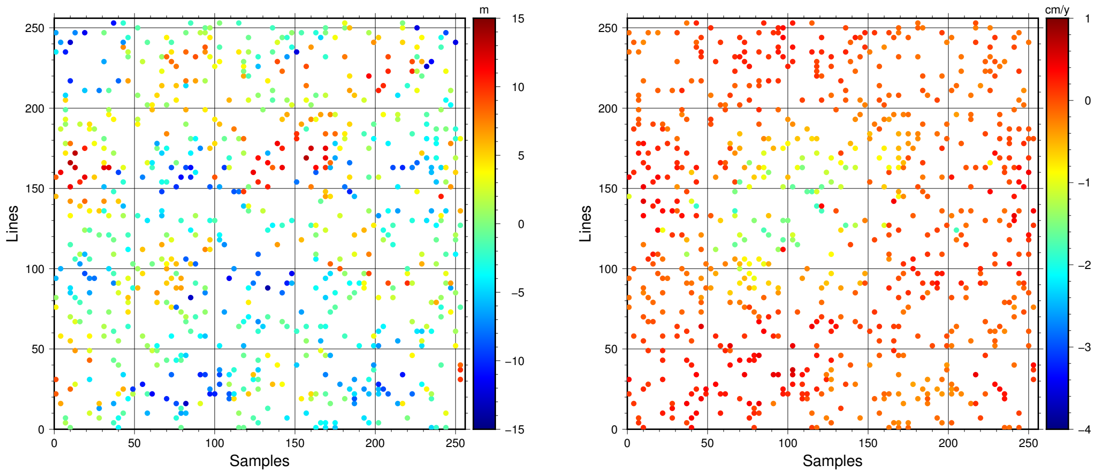

(a) (b)

Figure 5.8: Estimated DEM error (a) and linear velocity (b).

Initial Covariance estimation The first results are obtained using the default setting. Using the procedures previously described, the error on the phase is propagated to the estimated DEM error and velocity. The obtained maps are reported in 5.9a and 5.9b respectively.

First, observe that the standard deviation values are contained in a reasonable range: the velocity uncertainty is in the order of centimeters, being $\sigma_v \in [0, 0.252]$ cm, while the DEM error uncertainty is in the order of meters, $\sigma_\epsilon \in [0, 47]$ m. Second, the seed, whose variance is assumed to be zero, is clearly visible in both maps. Note the effect of the triangulation, that propagates the uncertainty of one pixel to the neighbours: it is particularly evident in the case of the seed, that influences the surrounding area decreasing the variance. From now on, only the velocity will be considered as the DEM error, being obtained using the same procedure, doesn't provide any additional information nor insight.

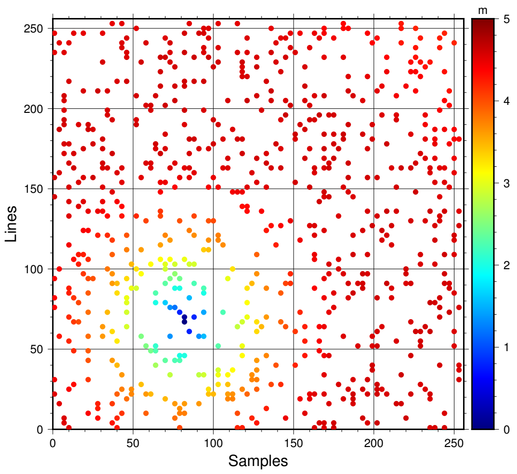

(a)

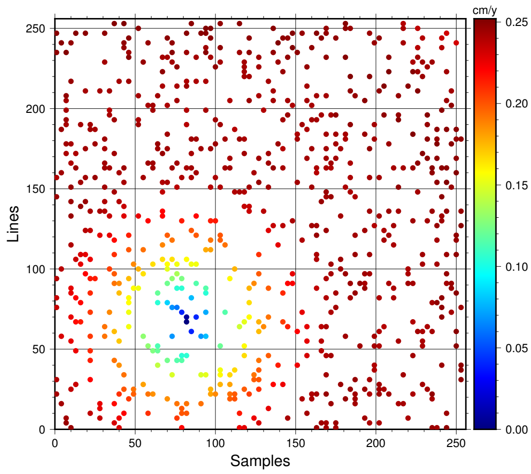

(b)

Figure 5.9: Estimated standard deviation for the DEM error (a) and for the linear velocity (b) of the selected pixels.

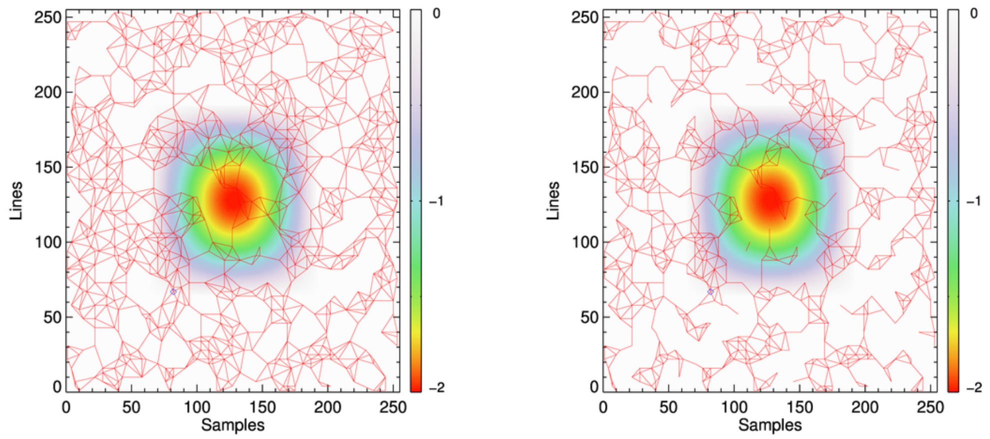

(a) (b)

Figure 5.10: Triangulation with maximum link length of 500 m (a) and 400 m (b).

Sensitivity to the density of the triangulation Two different triangulations, obtained imposing a maximum link length of 500 and 400 m, are used to test the results with different degrees of sparsity. The networks are reported in fig. 5.10a and 5.10b. The correspondent error maps are reported in fig. 5.11a and 5.11b.

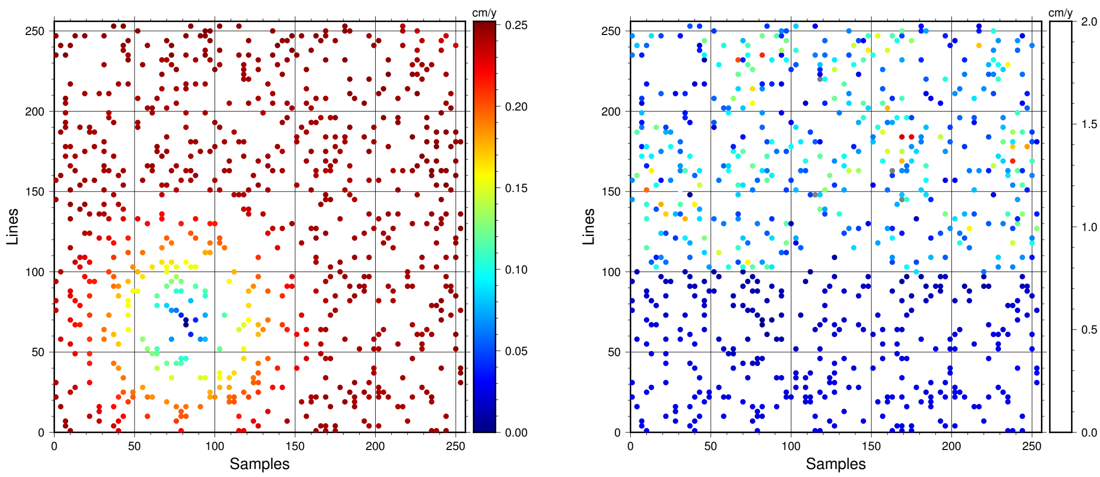

(a) (b)

Figure 5.11: Velocity standard deviation with maximum link length of 500 m (a) and 400 m (b).

The decreased number of links obtained in the first case does not affect significantly the standard deviation, that mantains values similar to the default scenario. On the contrary, the sparsity of the connections of the second configuration heavily impacts the error. This result, together with the ones obtained through other tests, allows to infer the existance of a maximum sparsity value over which the results can not be considered reliable.

Finally, in fig. 5.12 the standard deviation is plotted for each selected pixel. The pixel are ordered by rows, so their indices are correlated with the relative distance between them. Again, the effect of the seed on the neighbour pixels is clearly visible.

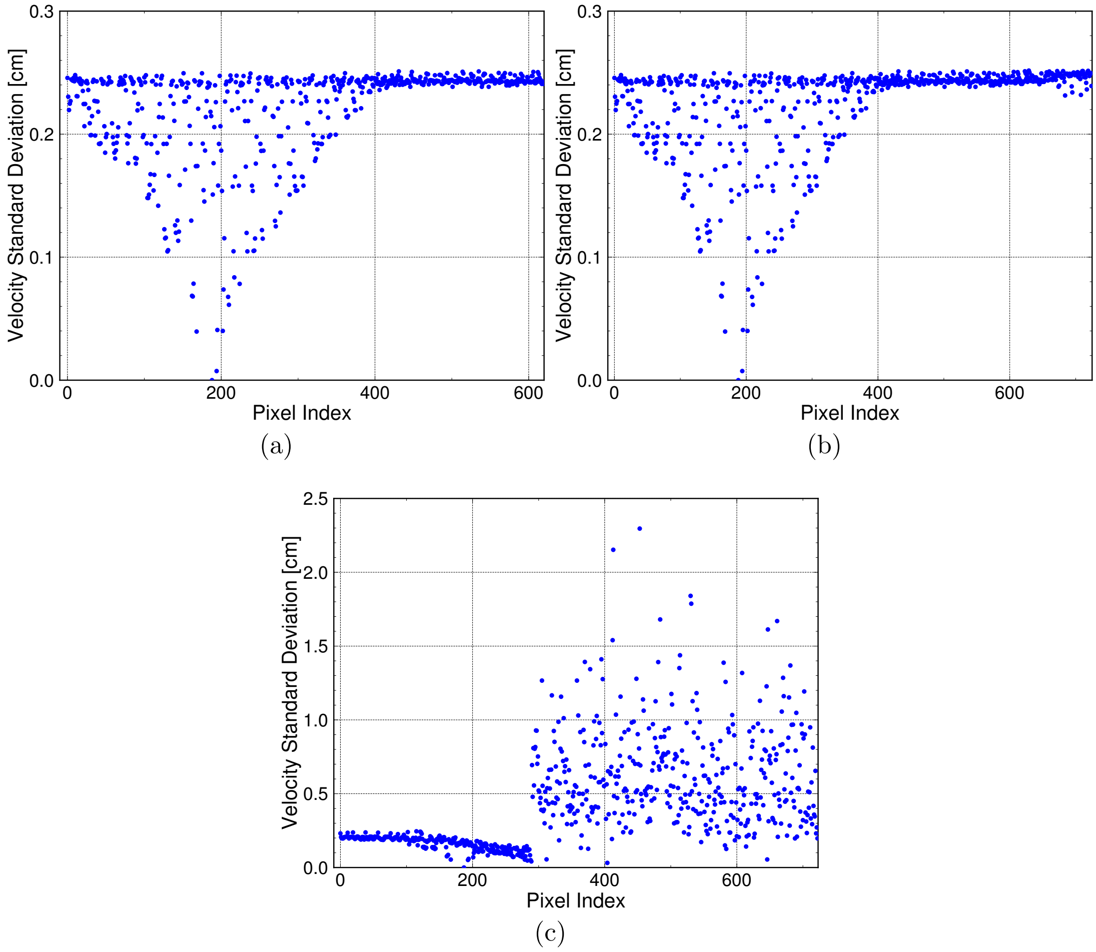

Figure 5.12: Velocity standard deviation with maximum link length of 800 m (a) 500 m (b) and 400 m (c).

Sensitivity to masking The behavior of the error is tested employing a mask, that tries to isolate the seed cancelling out some pixels and therefore modifying the relative distances with respect to the triangulation network. Two different masks are applied to the 800 m and 500 m triangulation previously introduced.

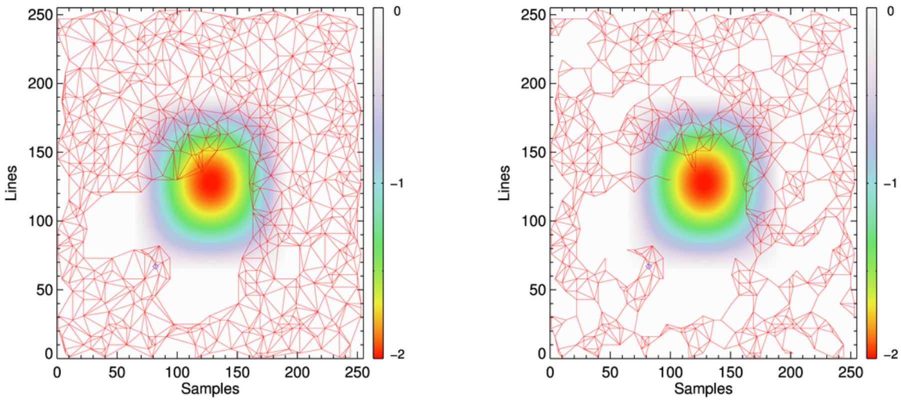

(a) (b)

Figure 5.13: Triangulation with maximum link length of 800 m (a) and 500 m (b) after the application of the mask.

The triangulations obtained applying the first mask are plotted in fig. 5.13a and fig. 5.13b. First, the effect of the masking on the estimated linear velocity should be considered. From fig. 5.14a and 5.14b it can be observed that this kind of mask does not heavily impact the estimation of the linear velocity in neither of the two cases.

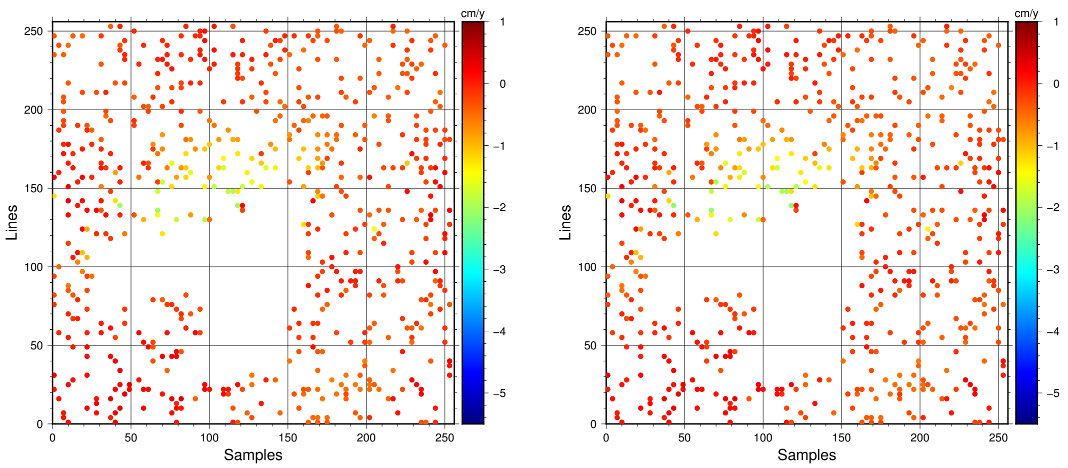

(a) (b)

Figure 5.14: Estimated linear velocity with maximum link length of 800 m (a) and 500 m (b) after the application of the mask.

The corresponding error patterns are reported in fig. 5.15 and in fig. 5.16. The result confirms what has already been noticed for the estimated velocity, i.e., the error is not significantly affected by the mask.

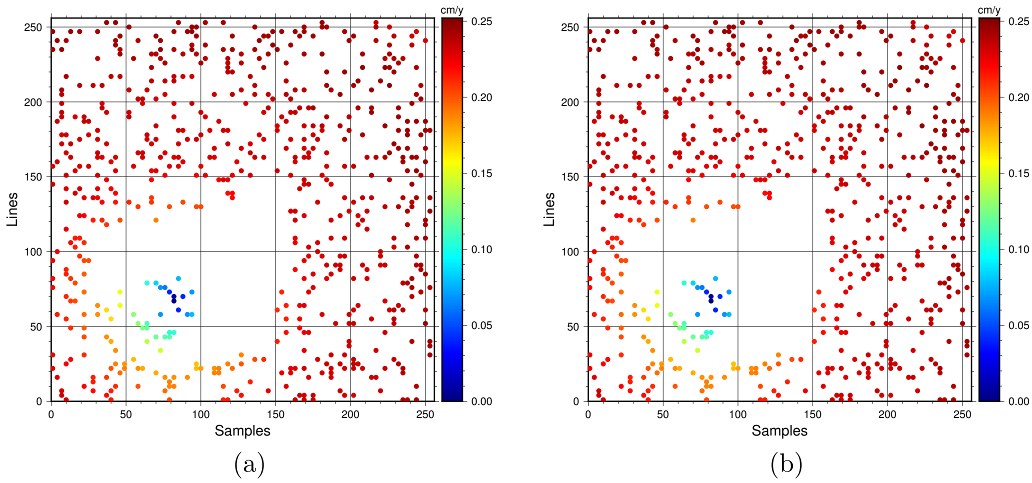

Figure 5.15: Estimated linear velocity standard deviation with maximum link length of 800 m (a) and 500 m (b) after the application of the mask.

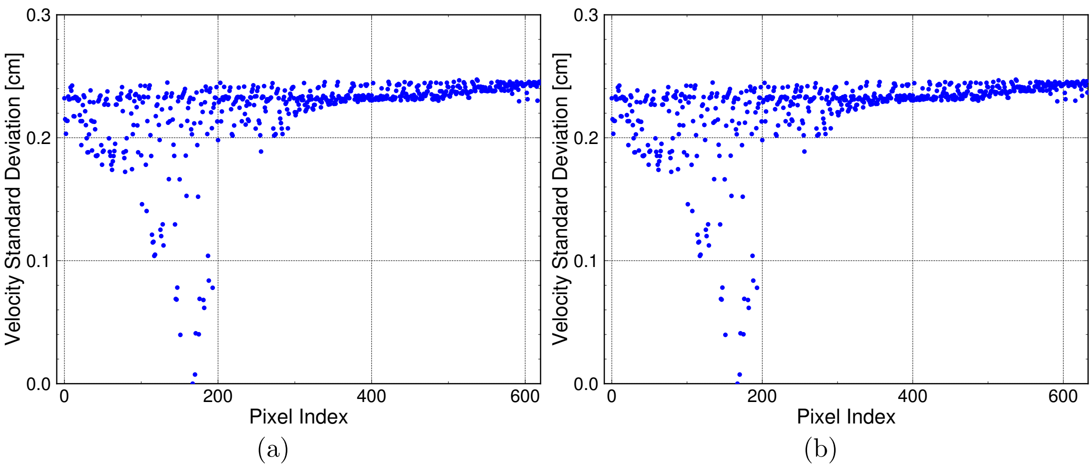

Figure 5.16: Velocity standard deviation with maximum link length of 800 m (a) and 500 m (b) after the application of the mask.

The same structure is followed for the results obtained applying the second mask. The new triangulations are plotted in fig. 5.17a and fig. 5.17b.

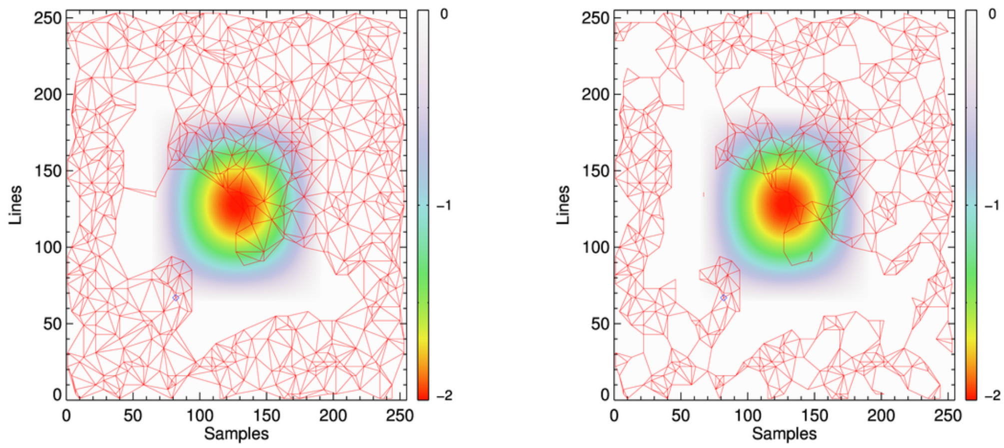

(a) (b)

Figure 5.17: Triangulation with maximum link length of 800 m (a) and 500 m (b) after the application of the second mask.

Again, the linear velocity results, reported in fig. 5.18a, don't present visible variations in the two triangulations. On the contrary, a significant variation is

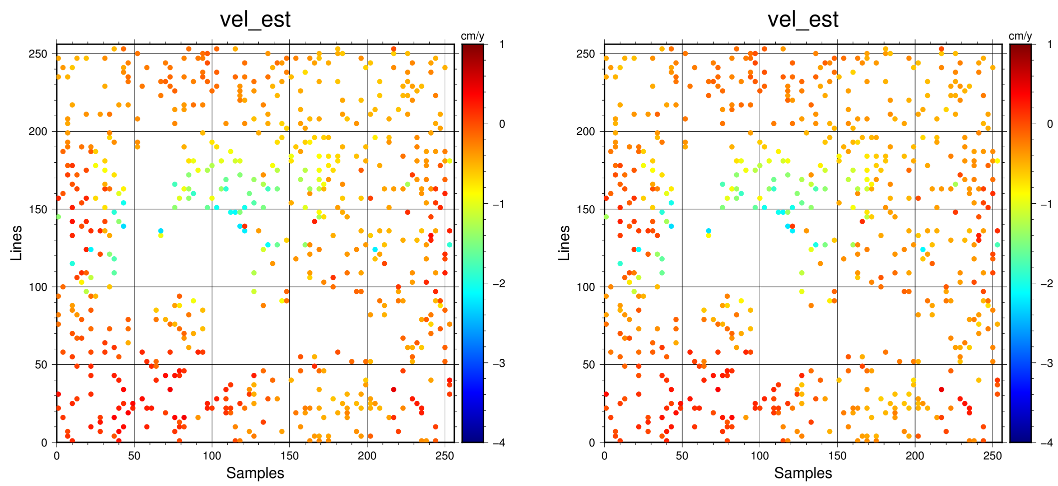

(a) (b)

Figure 5.18: Estimated velocity with maximum link length of 800 m (a) and 500 m (b) after the application of the second mask.

present in the error patterns, plotted in fig. 5.19a and in fig. 5.19b. Once again, the masking has a stronger impact on the sparser triangulation than on the denser one. The standard deviation of the estimated velocity reaches values that are even larger than the velocity itself, making it meaningless.

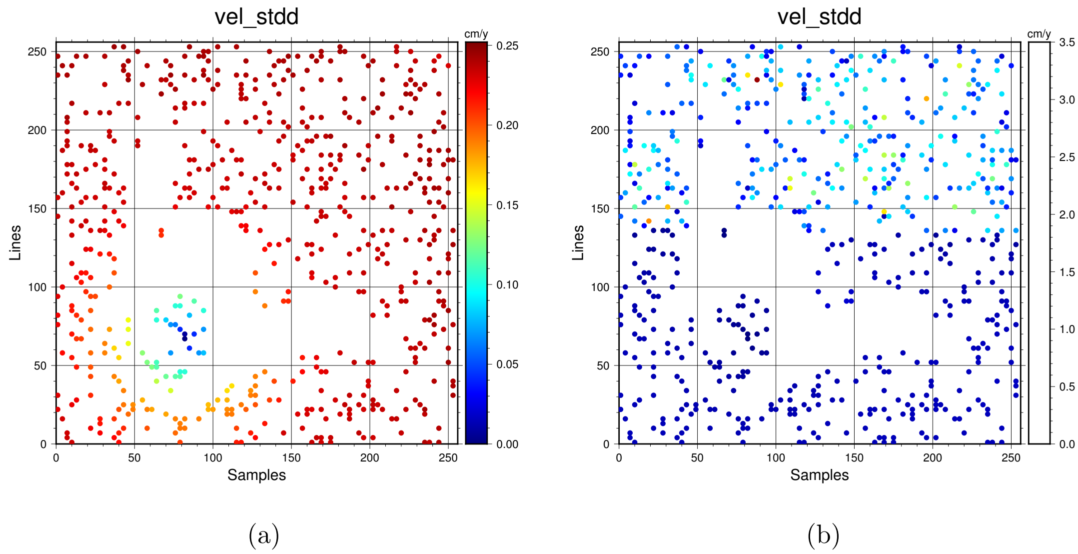

Figure 5.19: Estimated standard deviation velocity with maximum link length of 800 m (a) and 500 m (b) after the application of the second mask.

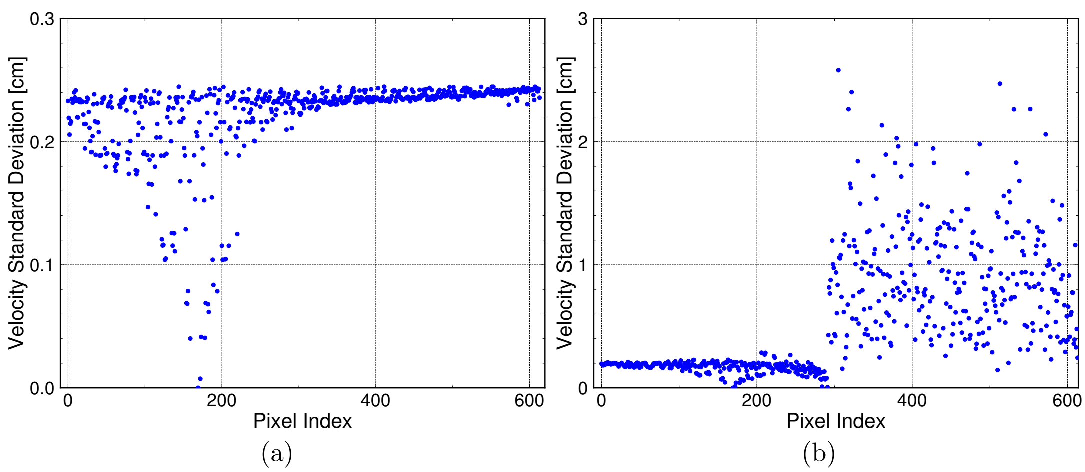

Figure 5.20: Velocity standard deviation with maximum link length of 800 m (a) and 500 m (b) after the application of the second mask.

Conclusions In this last section, the theory of the error propagation has been applied to a synthetic scenario, that is much easier to control than a real one. The model has been tested on a standard configuration, providing good results: the standard deviation of the estimated quantities assumes reasonable values, and the zero variance that characterizes the seed lowers the uncertainty of the neighbouring pixels. Several test have then provided useful insights on the behaviour of the error in different scenarios. The main variation across the tests regarded the triangulation and the density of links. From the correspondent results, it can be concluded that a good triangulation is fundamental for obtaining reliable results. The existence of a maximum sparsity, beyond which the estimated parameters become unreliable, has been inferred but remains to be demonstrated.

Chapter 6

Experimental evaluation: Venice subsidence

The city of Venice has a very unique history. Founded during the V century A.D. by the inhabitants of the nearby cities and countryside who were fleeing successive waves of barbarian invasions, the city is built on 118 small islands made stable by the hardening of the wooden platforms that support the buildings.

The city has suffered a slow subsidence during the centuries. Although in other scenarios these changes could be overlooked due to their small magnitude, they need to be taken into account when observing the city of Venice for its small elevation over the sea level. In case of high sea rises, the streets are flooded, an event called *acqua alta* ('high water'). It is therefore important to monitor with high accuracy the changes of the environment, and a measure of the reliability of these results is of primary importance.

The first section presents the data used for the interferometric processing. The rest of chapter is organized as the synthetic data section. First, the results of the estimation of the linear parameters are presented. Then, the error maps are obtained and a brief analysis is conducted. Finally, the results of a simple experiment are reported. This test is different from the ones of the previous section, as it exploits the peculiar topology of Venice. For brevity, only the results on the linear velocity are reported. As already mentioned, the results for the DEM error are analogous and don't bring any additional contribution.

6.1 Data specification and interferometric processing

The sensors chosen for the analysis of the Venice area are Sentinel-1 A and B of the European Space Agency (ESA). The two satellites employ the TOPS acquisition mode; in particular, the interferograms where generated selecting an area that contained three adjacent bursts [16].

Parameter	Value
Original Number of Images	35
Selected Number of Images	27
Original Size of the Images (pixels)	21349×13499
Multilook	3x11
Total number of interferograms	65
Maximum Spatial Baseline (m)	300.0
Maximum Temporal Baseline (days)	260
Size of the ROI (pixels)	6501×2001
Minimum Coherence Threshold	0.7
Percentage of Interferograms to Pass the Threshold	80%
Seed Position (sample, line)	(5027,1279)

Table 6.1: Venice initial input data.

Thirtyfive SLC images were obtained, one per month in the period between January 2015 and December 2017 (with the exception of May 2015, for which the image was not available). The geographic region of interest spans from (45.6284,12.022) (top left corner) to (45.2521,12.4221) (bottom right corner). Eight images had to be discarded as their overlap with the selected region was less than 67%. The high resolution image is reported in fig. 6.1.

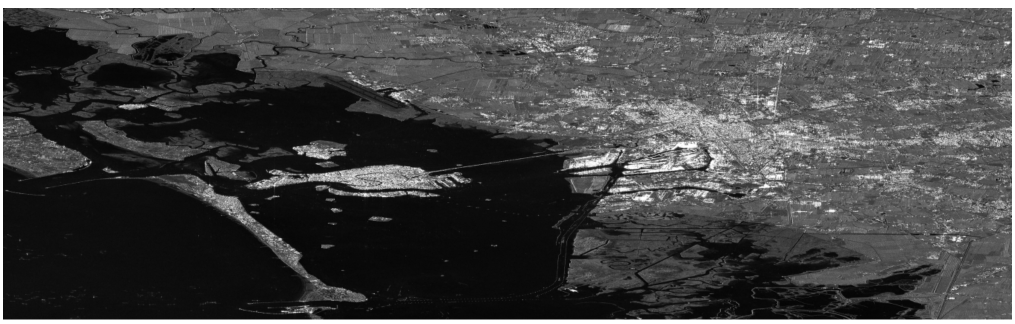

Figure 6.1: High resolution image of the selected area.

The image chosen as master was acquired on 11th March 2016. Sixtyfive interferograms were generated according to the triangulation plotted in fig. 6.2 and to the parameters of table 6.1. The study area was then further restricted to a smaller Region of Interest as specified in table 6.1 for computational reasons. Throughout all this chapter, the coherence method is used for the selection of the pixels, with the same minimum allowed coherence threshold, 0.7, and percentage of interferograms that need to satisfy it, 80%. The phase statistics are reported in 6.3. The maximum tolerated standard deviation is 0.1 radians.

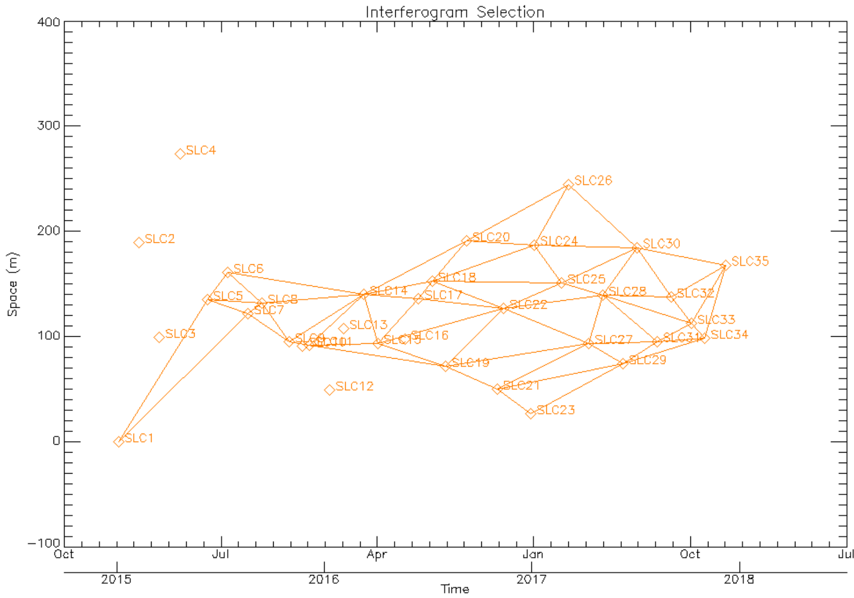

Figure 6.2: Selection of the SLC images for the generation of the interferograms.

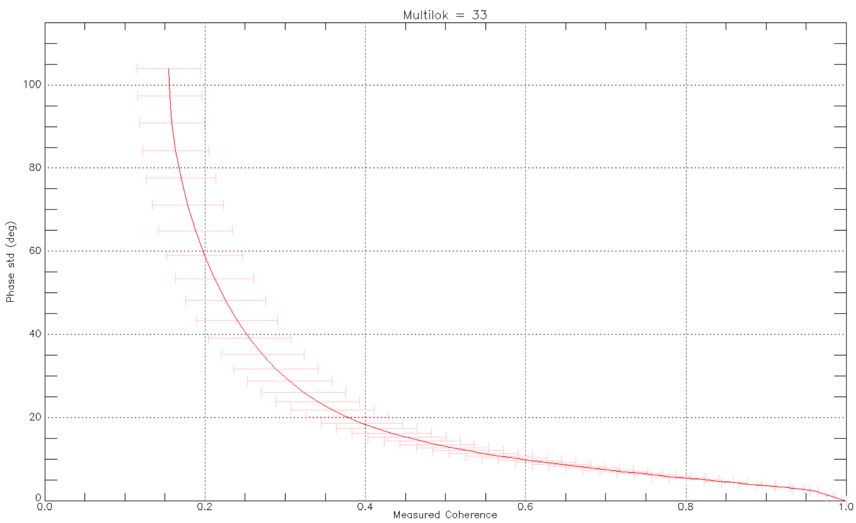

Figure 6.3: Phase standard deviation vs measured coherence.

6.2 Initial parameter estimation

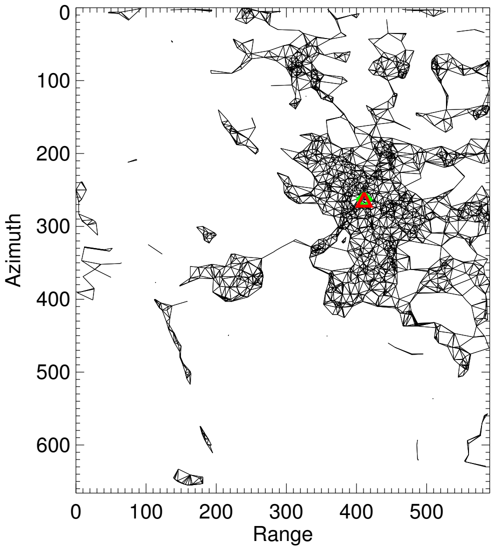

Figure 6.4: Initial Triangulation.

Parameter	Value
Num. of Interferograms	50
Max. Spat. Baseline (m)	200
Max. Temp. Baseline (days)	160
Num. of Selected Pixels	2232
Max. Num. of Relations	26
Num. of Relations	12496
Max. Link Distance (m)	800

Table 6.2: First configuration parameters.

The parameters for the first configuration are specified in table 6.2 and the obtained triangulation is plotted in 6.4, where the seed is also highlighted. Note that pixels containing regions of the sea are inevitably not selected, as the water surface can be considered, from the backscattering point of view, as a fully uncorrelated random process both in space and in time.

The estimated linear velocity is reported in fig. 6.5. The velocity values are referred to the seed placed in the mainland, in a point that is assumed to be stable ($v = 0$ [cm/yr]). Note that the displacement values are extremely low, in the order of millimeters, as expected. The scatterplot highlights the presence of some outliers that make the map visualization more difficult to read. The error map is depicted in 6.6. The realistic data present the same behaviour as the simulated one, as the neighbour pixels benefit of the seed presence exibiting a low uncertainty. On the contrary, points further apart suffer of a gradually increasing standard deviation. The seed position is clearly visible in both the plots.

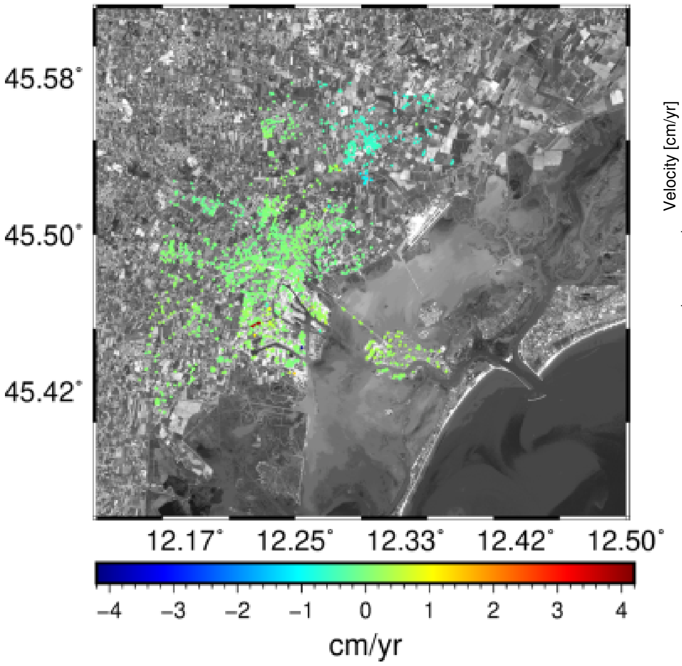

(a)

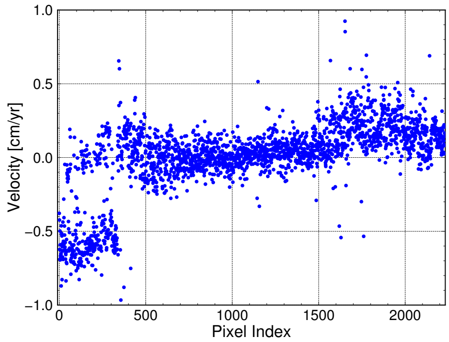

(b)

Figure 6.5: Linear velocity map (a) and scatterplot (b).

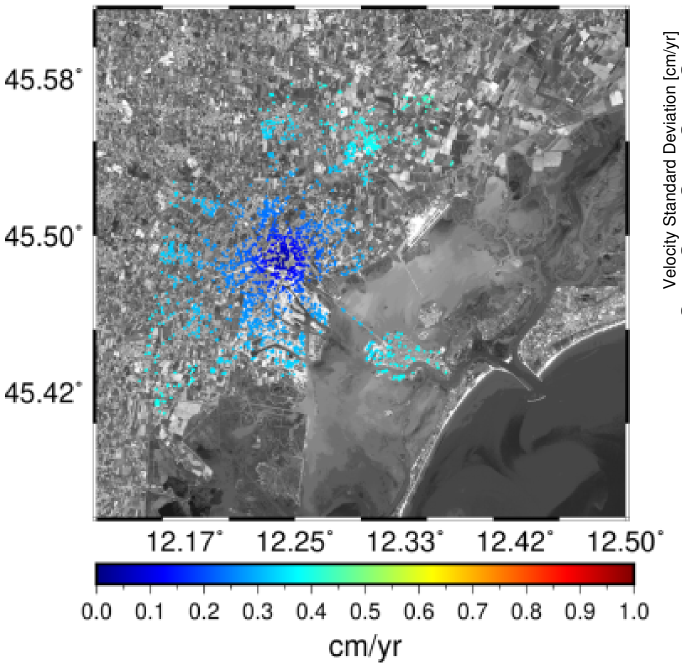

(a)

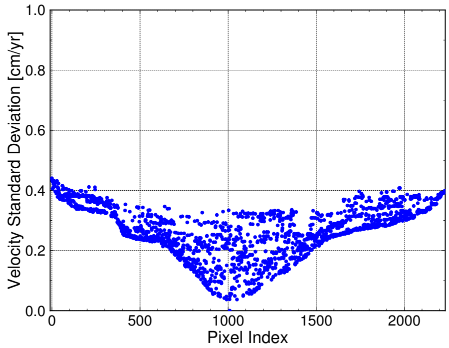

(b)

Figure 6.6: Linear velocity error map (a) and scatterplot (b).

6.3 Reduced number of interferograms

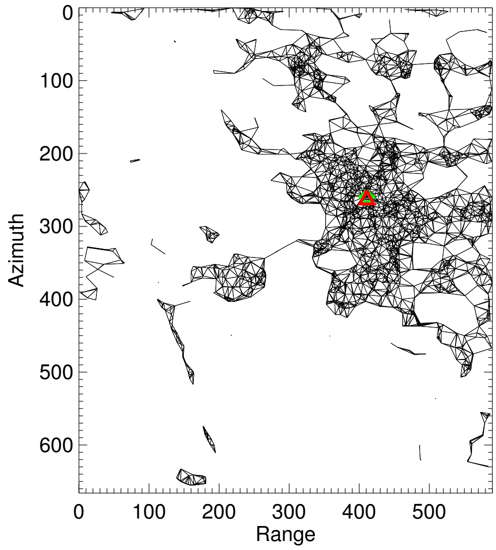

Figure 6.7: Triangulation obtained with a stack of 25 interferograms.

Parameter	Value
Num. of Interferograms	25
Max. Spat. Baseline (m)	200
Max. Temp. Baseline (days)	160
Num. of Selected Pixels	2791
Max. Number of Relations	27
Num. of Relations	15670
Max. Link Distance (m)	800

Table 6.3: Parameters obtained with a reduced set of interferograms.

The first test is done simply reducing the number of interferograms by half. One interferogram every two months is selected, starting from January 2015. The other parameters remained unchanged with respect to the previous setting. Clearly, a different number of pixels is selected, as reported in table 6.3, over which a new triangulation is performed.

The estimated linear velocity map is reported in fig. 6.5. The scatterplot in particular allows a clear view of the changes from the previous situation. Note that the new position of the seed in the selected pixels vector is just due to the new triangulation, as fig. 6.7 confirms that the geographical coordinates remain the same. The data present a higher dispersion and from the comparison with the previous model and with external information [15], the velocity appears to be overestimated for the leftmost cluster of pixels.

The theory developed in the previous chapters would suggest that a higher number of interferogram can guarantee a better result. The error plots in fig. 6.8 confirm it, as the error is indeed increased. The standard deviation of the just mentioned first cluster presents greater values, suggesting a lower reliability of the corresponding pixels. This gives credit to the previously formulated hypothesis that the new trend of the velocity in this region is overestimated.

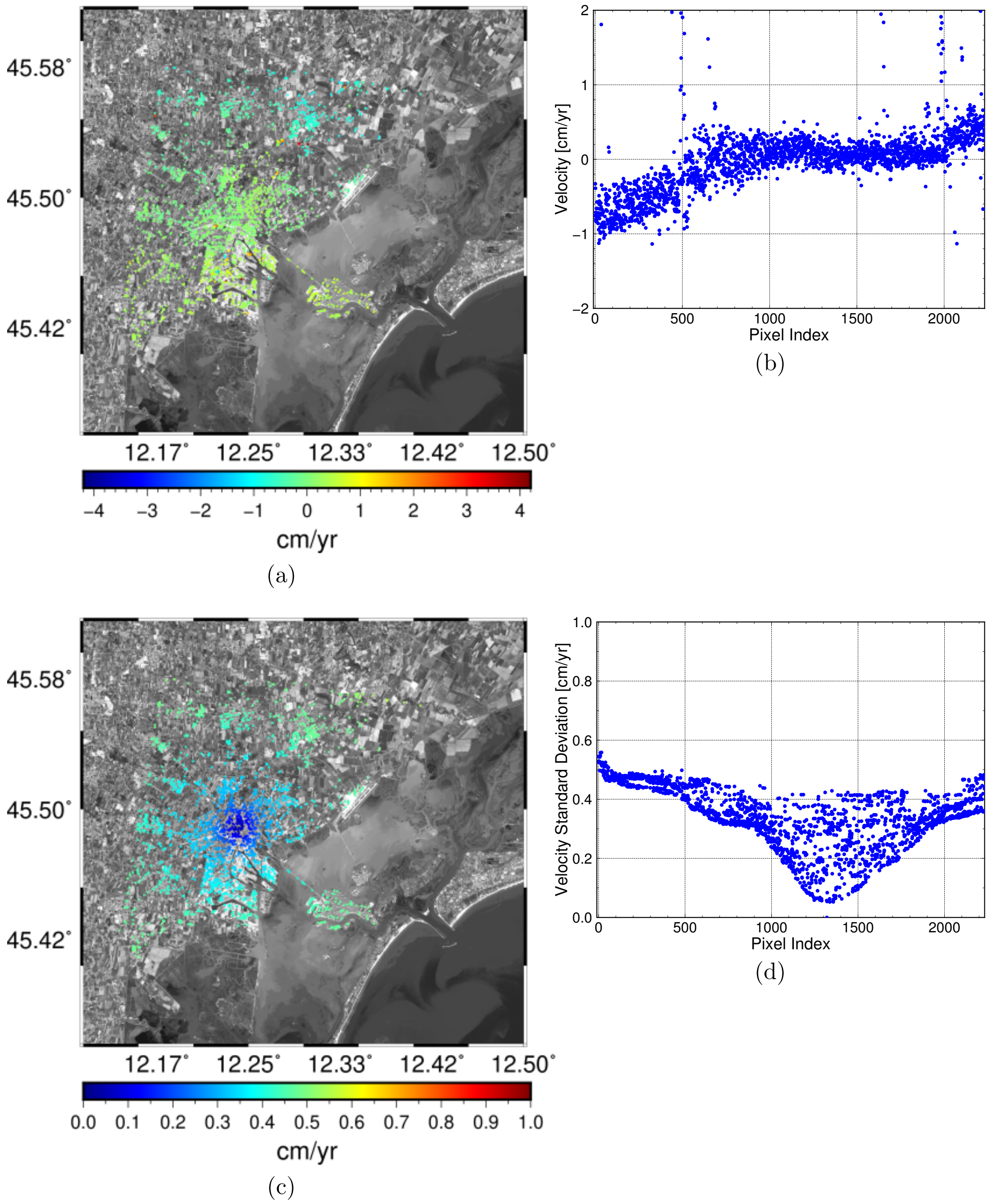

Figure 6.8: Linear velocity map (a) and scatterplot (b) and corresponding error map (c) and scatterplot (d).

6.4 Sparser triangulation

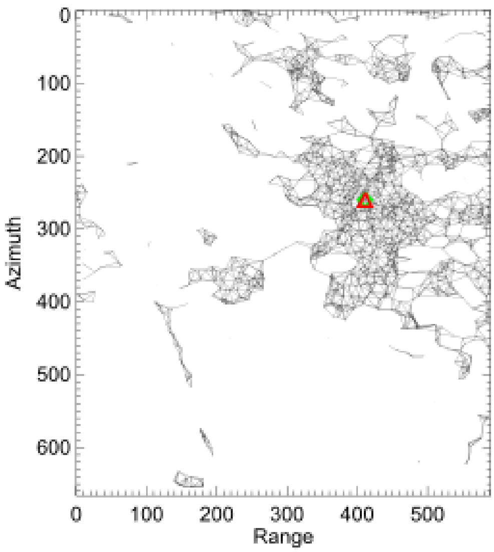

Figure 6.9: Triangulation obtained with a maximum link distance of 700 m.

Parameter	Value
Num. of Interferograms	25
Max. Spat. Baseline (m)	200
Max. Temp. Baseline (days)	160
Num. of Selected Pixels	2233
Max. Num. of Relations	27
Num. of Relations	12544
Max. Link Distance (m)	700

Table 6.4: Parameters obtained with a sparser triangulation.

The third scenario is built considering the same number of interferograms as in the previous case but a lower maximum link distance. This latter choice makes the trangulation sparser and this, in turn, completely isolates some of the pixels selected by means of the coherence criterion. The pixels without connections need to be discarded before the processing. The larger number of pixels in the setting with 25 interferograms was the reason behind this choice, as the final number of selected points guarantees that the city of Venice is still connected to the mainland.

The estimated linear velocity and the corresponding error are reported in fig. 6.10. Note that the standard deviation increases from the previous case but not in a significant way. It becomes difficult to compare the results with the one of the first scenario, as the pixel selection and thus the triangulation have changed once again. Since the coherence criterion and the considered geographical area are still the same, it is possible to observe a similar trend of the velocity in regions that can be considered similar or close, but further comparisons based on the scatterplot only would not be meaningful without a more in-depth study.

6.5 Spatial Error Propagation

On the 700 meter-scenario an interesting experiment can be conducted. Given the sparser connection network and the peculiar topography of the region, the

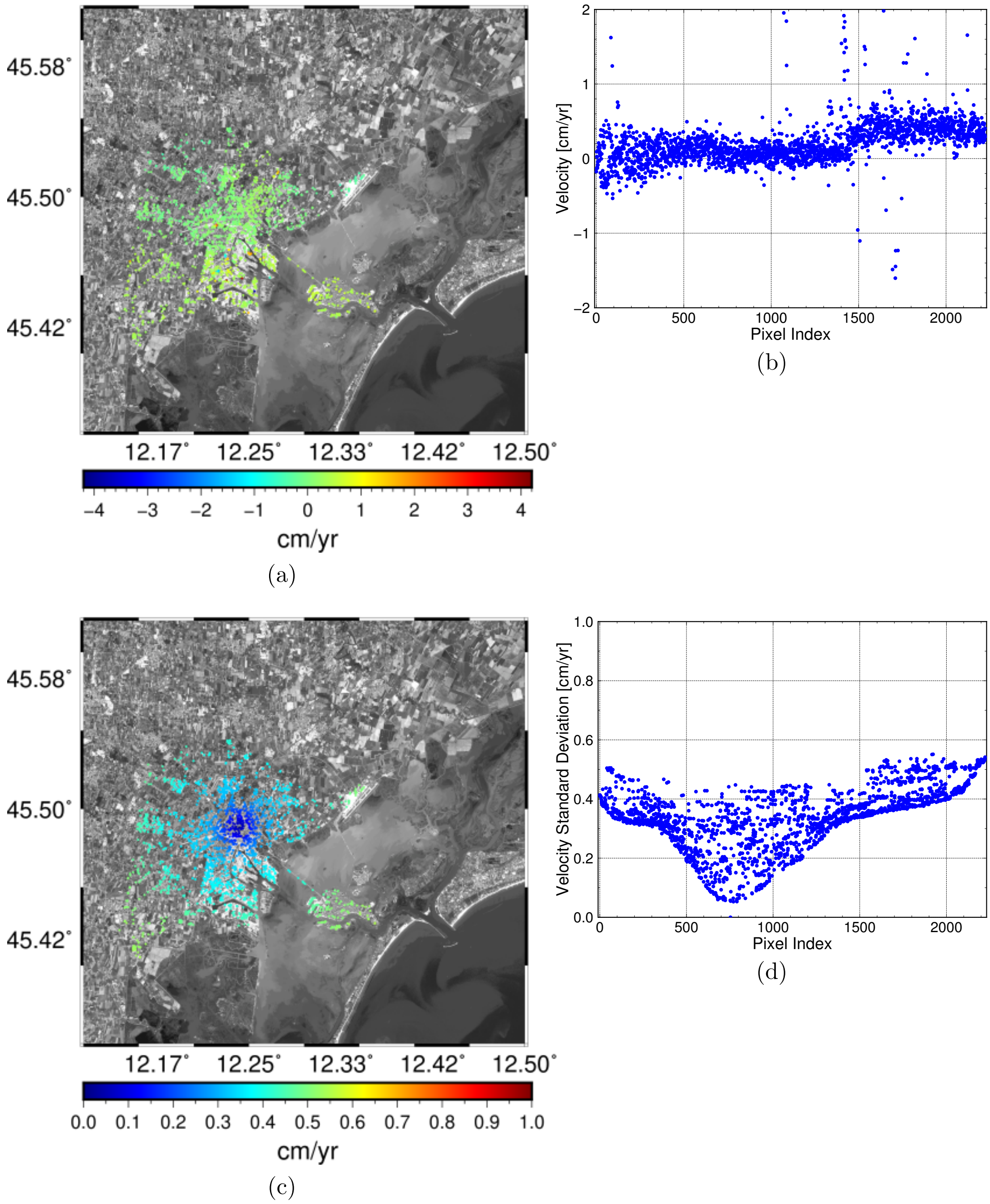

Figure 6.10: Linear velocity map (a) and scatterplot (b) and corresponding error map (c) and scatterplot (d).

city of Venice results in being connected to the mainland only by a few pixels distributed along the "Ponte della Libertà" bridge. As already mentioned, sea pixels are naturally discarded whereas the constraint on the links length further reduces the number of connections. In other words, the selected pixels form two clusters connected only through few nodes. It is then important to know the effects of the errors on these pixels, that from the triangulation graph point of view occupy a fundamental role, on the two clusters that they connect.

In order to study it, the same pixel selection and triangulation of the previous section are kept. A very high value, 1.714 [rad^2], is then artificially inserted in the phase covariance matrix in correspondance of the pixels of the bridge. This may seem an irrealistic scenario, since high variance pixels, with low coherence, wouldn't be selected during the pixel selection. Nevertheless, two considerations can be made. On one side, there are low-coherence scenarios in which the threshold needs to be adjusted in order to select a high enough number of pixels, accepting compromise on the quality of the results. On the other hand, the objective of this section is to study the spatial propagation of the errors through the Delaunay triangulation and the impact of the pixels in topologically relevant positions. Therefore, the high values injected work as "markers" that highlight the effects of the related changes.

The error map and standard deviation are plotted in 6.11. The effect of the errors is evident. Notice that the cluster containing the seed is not deeply affected; on the contrary, the error propagates from the bridge to the island, completely compromising it. The low variance of the seed doesn't propagate to the city of Venice, as this latter is connected ot the mainland only through the high variance pixels of the bridge.

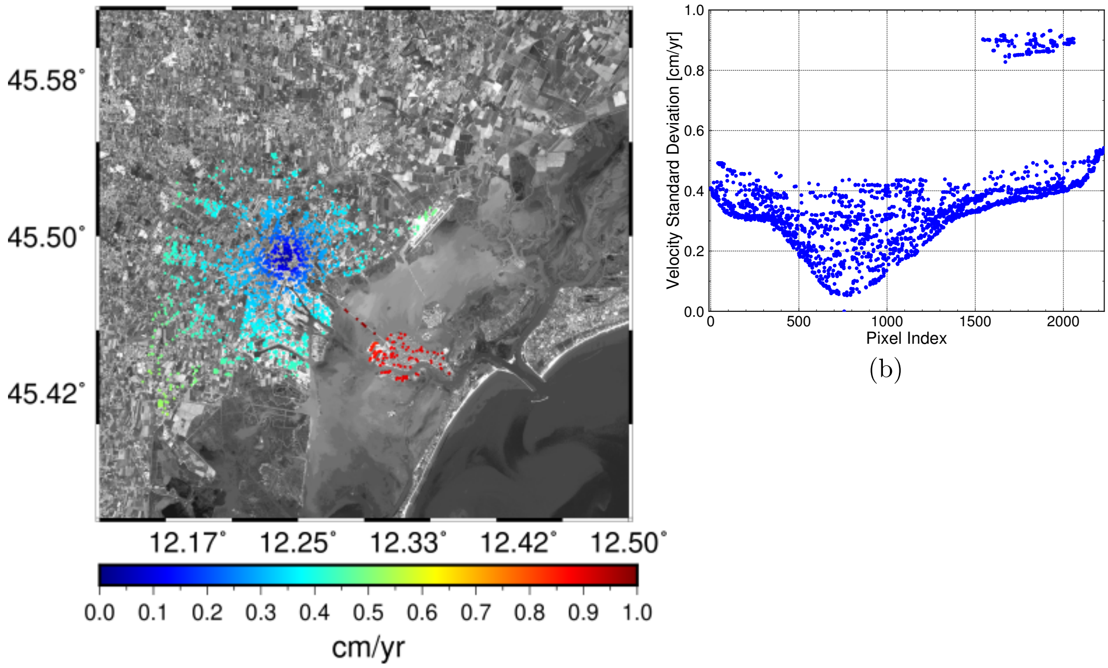

(a) (b)

Figure 6.11: Linear velocity error map (a) and scatterplot (b).

6.6 Conclusions

The focus of this chapter is on the study of the behaviour of the error in different, realistic, contexts, rather than on the estimation of the magnitude of the subsidence.

The results of the first section are used as a reference for both the linear velocity and the corresponding error. Its reliability is guaranteed by the high number of interferograms employed to determine the linear model.

This latter assumption is verified in the second section, where a lower number of interferograms significantly affects the quality of the results and the error.

The importance of employing a well-connected, dense triangulation, already found in the simulated environment, is confirmed by the worsening of the results in a sparser network.

Finally, the last scenario is indeed derived from the peculiar nature of Venice and the artificial tweaking of the Delaunay triangulation. Nevertheless, similar situations may arise in presence of highly vegetated areas, where town centers constitute coherent clusters that are connected only through the pixels of the roads, or in presence of islands. It is therefore of the most fundamental importance to pay extreme attention on the construction of the triangulation and on the quality of the pixels, especially of those connecting the clusters, as they might affect the results over an entire area.

Chapter 7

Conclusions

The first part of this work was devoted to presenting and analysing the basic remote sensing concepts needed as foundations for the remaining of the thesis. The Synthetic Aperture Radar concept was briefly discussed, followed by the explanation of how it can be employed to obtain useful images, called Single Look Complex (SLC) images, using spaceborn radars. The role of the SLC images in the construction of interferometric images is then analyzed, along with the topographic information that can be extracted from the latter. The introductory section was then concluded offering an overview of the Persistent Scatterer Interferometry technique, that allows the monitoring of land deformation.

The second part opened on these premises to deal with the stochastic characterization of the interferometric phase, that has been shown to play a central role in all interferometric applications. A complete model has been presented, dedicating special care to the quality parameters and the characterization of different kinds of targets. This allowed to proceed further into the analysis of the Coherent Pixel Technique (CPT) processing chain, that has been detailed to provide the necessary information for the last and most important part.

The novelty of this work was presented in its last part. The previously derived stochastic model of the interferometric noise was used as input to the CPT chain in order to retrieve the noise characterizing the output results, namely the DEM error and the deformation linear velocity. Building on a solid mathematical framework, the uncertainty of the results is obtained in term of their covariance, or, equivalently, their standard deviation.

The error propagation algorithm was firstly tested on a simulated scenario and secondly on a real one, in the area of the city of Venice. The objectives of the experiments were twofold: on the one hand, the pure testing of the proper working of the algorithm and of its implementation. On the other, its application in order to study the behaviour of the error in different scenarios. The algorithm provided results in line with the expectations: in particular, from a visual inspection the presence of the seed had noticeable effects on the neighbouring pixels through the triangulation. This latter was varied to obtain the different testing scenarios: the maximum link distance was modified to build sparser graphs and pixel masks where applied to artficially vary the network. The results showed that the triangulation has a significant impact on the uncertainty of the estimated quantities; in particular, some network topologies and densities have been shown to completely compromise the reliability of the results. This has been proved to be true also for the Venice dataset, that provided even clearer visualizations of these effects. The peculiar topography of Venice was then exploited to exibit an additional phenomenon: in presence of two clusters connected only by a small number of pixels, these latter play a central role and, if compromised, can affect the results on one whole area. A future line of work may follow to extend this on the non linear block of the CPT, providing analogous results for the time-series estimation uncertainty.

Drawing some final conclusions, the uncertainty propagation algorithm has been shown to be correct. As it is of primary importance for these applications, that measure the magnitude of deformations in the order of millimeters per year, to know the realiability of the results, the presented tool can be useful for a large number of users, producing reliability maps that should always be kept into considerations when working with the actual CPT results. As a second result, it opens future investigations on the behaviour of the error. The identification of particular triangulation topologies that compromise the reliability of the results can provide indications on whether an area can be analysed or not with a certain sensor. In situations where the pixels are clustered, the algorithm can point out the most sensitive areas as well as the most important pixels, for which a high reliability needs to be guaranteed. Many other considerations can follow and future researches will hopefully help the developing of the SAR interferometry field.

Appendix A

Optimization of the error propagation algorithm

This appendix is devoted to a brief explanation of the implementation of the error propagation procedure illustrated in chapter 5. It was deemed appropriate to spend some words on this as the matrices involved in the processing can have very large dimensions, making optimization a necessity.

The main idea behind the optimization is that there are two dimensions involved in the covariance matrices: on one hand, a "temporal dimension", as each interferogram can be considered as a snapshot of the area and they are distributed in the temporal and spatial baseline axes. On the other hand, a "spatial dimension" is determined by the pixels of a single interferogram or snapshot. For better highlighting the two dimensions, the elements of the matrix can be arranged in a stack of I matrices, each of dimension $P \times P$ and containing the variance-covariance values between pixels of a single interferogram. Thanks to this structure of the input covariance matrix, this two dimensions can be processed separately. In particolar, the most important characteristic of the interferometric pixels is their indipendence across the interferogram stack, that makes the submatrices of the block matrix in eq. (5.24) diagonal. Without this fundamental property, the following reasoning would not be possible.

Applying this reasoning first to the $(I \cdot P) \times (I \cdot P)$ input covariance matrix, one may observe that the "projection" of the matrix on the spatial plain would result in a $P \times P$ matrix containing the variance and covariance values of the selected pixels in a given interferogram. Notice that this new $P \times P$ matrix is dense and no longer diagonal.
Moving to the auxilary matrix necessary for the error propagation, consider first the pseudo-inverse in eq. (5.32). Matrix $\mathbf{G}$ is computed as a Kronecker product,

and therefore it is a block matrix that can be written as

$$\mathbf{G} = \mathbf{I}_L \otimes \mathbf{J} = \begin{bmatrix} \mathbf{J} & 0 & 0 & \cdots & 0 \\ 0 & \mathbf{J} & 0 & \cdots & 0 \\ \vdots & 0 & \ddots & \vdots & \vdots \\ 0 & \cdots & & & \mathbf{J} \end{bmatrix} \tag{A.1}$$

Each matrix $\mathbf{J}$ has dimension $I \times 2$. Notice that also in this case the $\mathbf{J}$ could be decomposed in the two planes, but a further optimization can be applied in order to reduce the computational load. Thanks to its block structure, the transpose of $\mathbf{G}$ can be directly computed as:

$$\mathbf{G}^T = \begin{bmatrix} \mathbf{J}^T & 0 & 0 & \cdots & 0 \\ 0 & \mathbf{J}^T & 0 & \cdots & 0 \\ \vdots & 0 & \ddots & \vdots & \vdots \\ 0 & \cdots & & & \mathbf{J}^T \end{bmatrix} \tag{A.2}$$

and the product $\mathbf{G}^T\mathbf{G}$ is the $(2 \cdot L) \times (2 \cdot L)$ block matrix

$$\mathbf{G}^T\mathbf{G} = \begin{bmatrix} \mathbf{J}^T\mathbf{J} & 0 & 0 & \cdots & 0 \\ 0 & \mathbf{J}^T\mathbf{J} & 0 & \cdots & 0 \\ \vdots & 0 & \ddots & \vdots & \vdots \\ 0 & \cdots & & & \mathbf{J}^T\mathbf{J} \end{bmatrix} \tag{A.3}$$

The computation of the inverse of the above product can be simplified as well, considering that

$$\left(\mathbf{G}^T\mathbf{G}\right)^{-1} = \begin{bmatrix} \left(\mathbf{J}^T\mathbf{J}\right)^{-1} & 0 & 0 & \cdots & 0 \\ 0 & \left(\mathbf{J}^T\mathbf{J}\right)^{-1} & 0 & \cdots & 0 \\ \vdots & 0 & \ddots & \vdots & \vdots \\ 0 & \cdots & & & \left(\mathbf{J}^T\mathbf{J}\right)^{-1} \end{bmatrix} \tag{A.4}$$

Finally, the whole $(L \cdot 2) \times (L \cdot I)$ pseudo-inverse is computed as

$$\begin{aligned} \left(\mathbf{G}^T\mathbf{G}\right)^{-1}\mathbf{G}^T &= \begin{bmatrix} \left(\mathbf{J}^T\mathbf{J}\right)^{-1}\mathbf{J}^T & 0 & 0 & \cdots & 0 \\ 0 & \left(\mathbf{J}^T\mathbf{J}\right)^{-1}\mathbf{J}^T & 0 & \cdots & 0 \\ \vdots & 0 & \ddots & \vdots & \vdots \\ 0 & \cdots & & & \left(\mathbf{J}^T\mathbf{J}\right)^{-1}\mathbf{J}^T \end{bmatrix} \\ &= \begin{bmatrix} \mathbf{G}_{pseudo}^{sub} & 0 & 0 & \cdots & 0 \\ 0 & \mathbf{G}_{pseudo}^{sub} & 0 & \cdots & 0 \\ \vdots & 0 & \ddots & \vdots & \vdots \\ 0 & \cdots & & & \mathbf{G}_{pseudo}^{sub} \end{bmatrix} \end{aligned} \tag{A.5}$$

Note that the pseudo inverse, that will be indicated with the symbol $\mathbf{G}_{pseudo}$, is still a block matrix, whose $2 \times I$ blocks $\mathbf{G}_{pseudo}^{sub}$ are all identical and can be computed just once in advance, saving a great amount of memory and time. Furthermore, note that the two dimensions mentioned at the beginning of the chapter can still be identified: each $\left[\left(\mathbf{J}^T\mathbf{J}\right)^{-1}\mathbf{J}^T\right]$ can be interpreted as a "stack" of 2-dimensional vectors containing information related to the baseline pairs (k_{T_i}, k_{B_i}) associated to each interferogram.

The importance of the diagonality of the covariance submatrices comes into play when multiplying the increment covariance matrix by the pseudo-inverse of $\mathbf{G}$. Note that the former is still a block matrix composed of diagonal matrices, as the conversion from linear phase to increment involves only linear combinations of the diagonal submatrices.

Consider then the $P \times P$ submatrix $\mathbf{\Sigma}_{\Delta}^{i,j}$ in position (i, j) of the increment matrix. As just mentioned, this matrix is still diagonal, and can be fully represented by its diagonal values. These latter can be collected in a $P \times 1$ vector $\mathbf{\Sigma}_{Delta,diag}^{i,j}$. The left multiplication of the increment covariance matrix by the pseudo-inverse can then be written as

$$\mathbf{G}_{pseudo}\mathbf{\Sigma}_{\Delta} = \begin{bmatrix} \mathbf{G}_{pseudo}^{sub}\mathbf{\Sigma}_{\Delta}^{1,1} & \mathbf{G}_{pseudo}^{sub}\mathbf{\Sigma}_{\Delta}^{1,2} & \cdots & \mathbf{G}_{pseudo}^{sub}\mathbf{\Sigma}_{\Delta}^{1,P} \\ \mathbf{G}_{pseudo}^{sub}\mathbf{\Sigma}_{\Delta}^{2,1} & \mathbf{G}_{pseudo}^{sub}\mathbf{\Sigma}_{\Delta}^{2,2} & \cdots & \\ \vdots & & \ddots & \vdots \\ \mathbf{G}_{pseudo}^{sub}\mathbf{\Sigma}_{\Delta}^{P,1} & \cdots & & \mathbf{G}_{pseudo}^{sub}\mathbf{\Sigma}_{\Delta}^{P,P} \end{bmatrix} \tag{A.6}$$

where each submatrix is a can be computed just using an elementwise product between each of the two rows of $\mathbf{G}_{pseudo}^{sub}$ and $\mathbf{\Sigma}_{\Delta,diag}^{i,j}$ thanks to diagonality of the second matrix. The result is a $2 \times I$ submatrix. Considering the whole expressione for the linear increments matrix $\mathbf{\Sigma}_{\Delta v,\Delta\epsilon}$, obtained from eq. A.6 right-multiplying by the transpose of the pseudo-inverse matrix. Note that each row of the new matrix is computed as the sum of elements with structure

$$\mathbf{G}_{pseudo}^{sub}\mathbf{\Sigma}_{\Delta}^{i,j}\left(\mathbf{G}_{pseudo}^{sub}\right)^T \tag{A.7}$$

From the above considerations, eq. (A.7) can be rewritten as

$$\mathbf{K} = \left(\mathbf{G}_{pseudo}^{sub}\mathbf{\Sigma}_{\Delta,diag}^{i,j}\right)\left(\mathbf{G}_{pseudo}^{sub}\right)^T \tag{A.8}$$

where the left term has already been analysed. Note that the final result is a 2×2 matrix and the only important terms are the diagonal ones, representing the variance of the velocity and DEM error rispectively. Therefore, considering e.g. the first element of velocity increment variance, that is computed multypling the first row of $\mathbf{K}$ by the first column of $\left(\mathbf{G}_{pseudo}^{sub}\right)^T$, the following expression holds:

$$
\begin{aligned}
\mathbf{\Sigma}_{\Delta v,0} &= \begin{bmatrix} K_0 & K_1 & \cdots & K_{I-1} \end{bmatrix} \begin{bmatrix} \left[\mathbf{G}^{sub}_{pseudo}\right]_{0,0} \\ \vdots \\ \left[\mathbf{G}^{sub}_{pseudo}\right]_{0,I-1} \end{bmatrix} = \\
&= \begin{bmatrix} \left[\mathbf{G}^{sub}_{pseudo}\right]_{0,0} \left[\mathbf{\Sigma}^{i,j}_{\Delta,diag}\right]_{0,0} & \cdots & \left[\mathbf{G}^{sub}_{pseudo}\right]_{0,I-1} \left[\mathbf{\Sigma}^{i,j}_{\Delta,diag}\right]_{0,I-1} \end{bmatrix} \begin{bmatrix} \left[\mathbf{G}^{sub}_{pseudo}\right]_{0,0} \\ \vdots \\ \left[\mathbf{G}^{sub}_{pseudo}\right]_{0,I-1} \end{bmatrix} \\
&= \sum_{i=0}^{I-1} \left[\mathbf{G}^{sub}_{pseudo}\right]^2_{0,i} \left[\mathbf{\Sigma}^{i,j}_{\Delta,diag}\right]_{0,i}
\end{aligned}
\tag{A.9}
$$

from which two observations can be done: first, the matrix product can be substituted by a much easier sum of the elements of a column multiplied by a constant scalar; second, it is this operation that performs the projection of the time (interferogram) dimension on the image plane. From now on, all the matrices are thus defined only for one image, differently whereas up to this point they kept the "stacked" structure. Practically, this means that the remaining part of the algorithm needs much less memory and therefore optimization.

This reasoning basically allows to perform the computation using just one interferogram at the time, greatly reducing the memory requirements. In this way, in case of large clusters of selected pixels or highly connected triangulation it is possible to save the interferograms on the disk memory, avoiding the more stringent limitations imposed by the RAM memory.

Bibliografy

[1] https://sentinel.esa.int/web/sentinel/technical-guides/sentinel-1-sar/sar-instrument/acquisition-modes

[2] DE ZAN, Francesco; GUARNIERI, AM Monti. *TOPSAR: Terrain observation by progressive scans*. IEEE Transactions on Geoscience and Remote Sensing, 2006, 44.9: 2352-2360.

[3] HANSSEN, Ramon F. *Radar interferometry: data interpretation and error analysis.* Springer Science & Business Media, 2001.

[4] https://rsde.fbk.eu/research/synthetic-aperture-radar-SAR

[5] JUST, Dieter; BAMLER, Richard. *Phase statistics of interferograms with applications to synthetic aperture radar*. Appl. Opt. 33, 1994, 4361-4368.

[6] GUARNIERI, A. M.; PRATI, C. *SAR interferometry: a "Quick and dirty" coherence estimator for data browsing*, in IEEE Transactions on Geoscience and Remote Sensing, vol. 35, no. 3, pp. 660-669, May 1997.

[7] ABDELFATTAH, R.; NICOLAS, J. M. *Coherence estimation from complex coherence map using second kind statistics*, IEEE International Conference on Image Processing 2005, 2005, pp. II-229-32..

[8] ZEBKER, H. A.; VILLASENOR, J. *Decorrelation in interferometric radar echoes*, in IEEE Transactions on Geoscience and Remote Sensing, vol. 30, no. 5, pp. 950-959, Sep 1992.

[9] KASS, Robert E. *Nonlinear regression analysis and its applications.* Journal of the American Statistical Association, 1990, 85.410: 594-596.

[10] CENTOLANZA, Giuseppe, "Quality evaluation of DInSAR results from the phase statistical analysis", Doctoral thesis, Oct 2015. Universitat Politècnica de Catalunya. Departament de Teoria del Senyal i Comunicacions.

[11] EMARDSON, T. R.; SIMONS and M.; WEBB, F. H. *Neutral atmospheric delay in interferometric synthetic aperture radar applications: Statistical description and mitigation.* Journal of Geophysical Research: Solid Earth, 2003, 108.B5.

[12] https://en.wikipedia.org/wiki/Variogram

[13] KNOSPE, Steffen; JONSSON, Sigurjon. *Covariance estimation for dIn-SAR surface deformation measurements in the presence of anisotropic atmospheric noise.* IEEE Transactions on Geoscience and Remote Sensing, 2010, 48.4: 2057-2065.

[14] GNEITING, Tilmann; SASVÁRI, Zoltán; SCHLATHER, Martin. *Analogies and correspondences between variograms and covariance functions.* Advances in Applied Probability, 2001, 33.3: 617-630.

[15] TOSI, Luigi; TEATINI, Pietro; STROZZI, Tazio. *Natural versus anthropogenic subsidence of Venice.* Scientific reports, 2013, 3: 2710.

[16] YAGÜE-MARTÍNEZ, Néstor, et al. *Interferometric processing of Sentinel-1 TOPS data.* IEEE Transactions on Geoscience and Remote Sensing, 2016, 54.4: 2220-2234.

Thanks